Friction Identification on the Gantry Stage

Lan Jia
5468094

TU Delft

Friction Identification on the Gantry Stage

Thesis report

by

Lan Jia
5468094

to obtain the degree of Master of Science
at the Delft University of Technology
to be defended publicly on September 27, 2023

Thesis committee:

Chair:	Dr. Raj Thilak Rajan
Examiner:	Ir. Remon Damen
Examiner:	Dr. Alessandro Cabboi
Examiner:	Prof. Dr. Ir. Alle-Jan van der Veen
Project Duration:	November 2022 - September 2023

Faculty of Electrical Engineering, Mathematics and Computer Science · Delft University of Technology

Abstract

In an era marked by the demand for unprecedented levels of precision in engineering applications, the profound impact of friction forces on motion control systems cannot be underestimated. This thesis extensively investigates the frictional behavior of the Proton Motion Stage, an advanced high-precision motion control system developed by Prodrive Technologies. This research conducts both experimental investigations and computational simulations, offering valuable insights into its friction behavior across diverse conditions and scenarios.

The research begins with an analysis of existing models used to describe friction behavior in precision engineering systems. A critical evaluation of empirical models highlighting strengths and limitations is presented, and the LuGre friction model is selected. Subsequently, a simulation work is conducted to identify the viscous coefficients, the stiffness coefficient, the Coulomb friction, the Stribeck friction, and the Stribeck velocity in the LuGre model. The simulation setup is described, including the incorporation of the LuGre friction model and the identification of system parameters. The accuracy of the identification value to the true value is above 99%. A comparison of the sensitivity of the objective function to the change of parameters is also conducted to enable a comprehensive exploration of friction dynamics. Finally, the research delves into static and dynamic parameter experiments, where cable slab forces' position-dependent impacts and velocity-friction maps that capture the intricate Stribeck effect are presented, and closed-loop and open-loop setups to dissect friction behavior during rapid motion changes are employed. Residual analysis of histogram and 90% confidence autocorrelation and cross-correlation is also presented to study the quality of identification and shows that the LuGre model does not fully capture the friction phenomena on the Proton Motion Stage. Future research should involve the modification of the LuGre model and data-driven approaches such as machine learning. Overall, this thesis fills the gap in state-of-the-art works by combining theory and practice to enhance the understanding of friction in precision engineering systems.

Acknowledgements

At the end of my master's thesis, I would like to express my appreciation to those who helped me through this amazing journey.

First and foremost, I extend my gratitude to my thesis supervisor and the chair of the thesis committee, Dr. R.T. Rajan. Through the project, we had meetings where we had inspiring discussions about the progress and obstacles. I want to thank you for sharing your wisdom and guiding me during my graduation project.

Secondly, I would express my gratitude to Prodrive Technologies, without which this thesis would not have been possible. Special thanks to my daily supervisor Ir. Remon Damen for your guidance along the project. The interesting discussions and your constructive feedback have contributed significantly to my growth. Also, I would like to thank my colleagues for providing insightful advice for my project.

Last but not least, I would like to thank my parents, my cat, my boyfriend, and my friends for their emotional support during my master's study.

Lan Jia
Delft, the Netherlands
19 September 2023

Contents

List of Figures **v**

1 Introduction **1**
- 1.1 Background and Motivation 1
- 1.2 Objective 2
- 1.3 Outline 2

2 Literature Review **4**
- 2.1 Static Friction Models 4
- 2.2 Dynamic Friction Models 8
- 2.3 A Comparison of Friction Models 12

3 Parameter Identification **14**
- 3.1 Introduction 14
- 3.2 LuGre Model and Parameters 14
- 3.3 Methodology 15
- 3.4 Simulation Results 18
- 3.5 Summary 22

4 Experiments **23**
- 4.1 Experiment Setup 23
- 4.2 Identification of Cable Slab Force 24
- 4.3 Static parameter experiments 26
- 4.4 Dynamic parameter experiments 33
- 4.5 Summary 40

5 Conclusions and Future Work **42**

List of Figures

1.1 Proton Motion Stage from Prodrive Technologies. 2

2.1 Static friction models. 5
2.2 Regime 1: static friction. 6
2.3 Regime 2,3, and 4 in Stribeck curve. 7
2.4 Generalized Stribeck curve. 7
2.5 Bristles model to describe contact surface [5] 8
2.6 LuGre simulation results: (a) applied external force, (b) resulting position, (c) resulting position-force relationship. 9
2.7 Experimental results: (a) applied torque, (b) resulting angular position, (c) resulting position-torque relationship. 9
2.8 Maxwell Slip model for N elements 11
2.9 Maxwell Slip model for N massless elements. 12

3.1 Initial guesses of static parameters on velocity-friction map. 17
3.2 Velocity vs time with maximum velocity set to 0.001m/s. 18
3.3 The velocity inputs for static and dynamic parameter identification. 19
3.4 LM method simulation. 20
3.5 Sensitivity of objective function to changes of static and dynamic parameters. 21
3.6 Probability density function of parameters from 100 Monte-Carlo trails. 22

4.1 Proton Motion Stage from Prodrive Technologies. 23
4.2 Relevant forces. 24
4.3 Cable slab force at position range [-0.15m,0.15m]. 25
4.4 Indication of cable slab and carrier. The cable slab is shown as red lines, and the carrier is shown as the blocks. 26
4.5 To avoid the impact of the transition period, the carrier is controlled to move twice the effective distance, and only the latter half is considered effective. 27
4.6 Velocity-friction map for static parameter identification at position -0.136m. 28
4.7 Stribeck effect at position -0.136m. 29
4.8 Velocity-friction map for static parameter identification at different positions. 29
4.9 Identification results at 9 positions. 30
4.10 Histogram of residuals after identification at position 0. 31
4.11 Analysis of identification result at position 0. 32
4.12 Closed-loop experiments to achieve velocity reversal. 33
4.13 Closed-loop experiment for dynamic parameters. 34
4.14 Identification of dynamic friction under closed-loop control system at position 0. 35
4.15 Identification results at 9 positions. 37
4.16 Identification results at 0.102m 38
4.17 Histogram of residuals after identification at position 0.102. 39
4.18 Analysis of identification result at position 0.102.. 40

1
Introduction

1.1. Background and Motivation

In the realm of precision engineering, due to the rapid developments in technology, achieving high levels of accuracy has become crucial. Nonetheless, a challenge arises from the presence of disturbance forces within precision systems, and frequently results in deviations from accurate tracking and positioning [1] [2]. Among these disturbance forces, friction force plays a prominent role. For control of precision engineering, the friction force is an unwanted and intricate phenomenon that introduces nonlinear characteristics, subsequently giving rise to control-related issues [2]. Notably, the friction force is a major contributor to problems like stick-slip, significantly impacting the overall tracking performance of precision systems. To eliminate friction force in precision engineering, designs such as air bearings and magnetic bearings are used. For some scenarios that require performances with higher precision, effectively identifying friction force and thus compensating friction force is needed to ensure the desired levels of accuracy [3][4].

A widely utilized approach to address friction force identification is through model-based methodologies. Model-based methodologies use models that encompass friction in both situations with and without a relative movement and strive to describe the complex behavior of friction within precision engineering systems [3][4]. Among the options explored, the LuGre friction model [5] emerges as a significant choice. It offers a comprehensive representation of frictional effects by combining elements of Coulomb friction, viscous friction, and stick-slip effect, allowing it to capture both static and dynamic friction phenomena [2]. In addition to the LuGre model, the Leuven model [6], the Modified Leuven model [7], and the Generalized Maxwell Slip model (GMS) [8] are also noteworthy models of friction force. The Leuven model focuses on simulating dynamic friction behavior, incorporating features such as non-local hysteresis characteristics [6]. The Modified Leuven model expands upon the Leuven model's foundation, updating its representation of friction dynamics [7]. Lastly, the GMS model introduces the analogy of multiple viscoelastic elements to account for the viscoelastic properties of friction materials [9]. These friction force models collectively serve as indispensable tools for the understanding and modeling of friction force phenomena, and are promising to be used in mitigating the challenges posed by friction forces in precision engineering systems [8].

The Proton Motion Stage in Figure 1.1, developed by Prodrive Technologies, showcases cutting-edge engineering in the field of motion control. This high-precision motion system is a complex mix of mechanical components, sensors, and control algorithms that work together to achieve precise movements with great accuracy. However, in such complex systems, friction becomes a critical factor that can impact performance, accuracy, and overall system behavior. The success of the Proton Motion Stage depends on its ability to overcome the challenges posed by friction, making a comprehensive investigation into its frictional characteristics a matter of utmost importance.

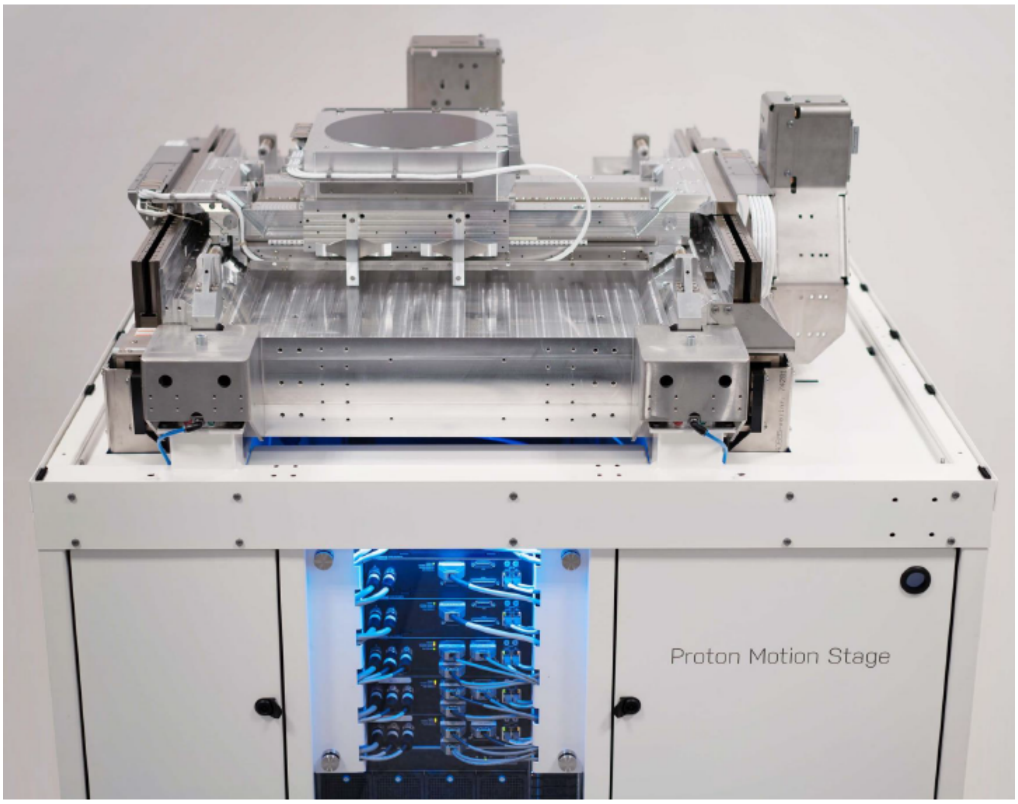

Figure 1.1: Proton Motion Stage from Prodrive Technologies.

This thesis aims to provide insights into the friction force within the context of the Proton Motion Stage, and thus offer knowledge that can inform the design, optimization, and operation of the Proton Motion Stage and similar precision engineering systems.

1.2. Objective

The primary objective of this thesis is to select a suitable friction model and to identify the friction parameters of the Proton Motion Stage, with the aim of enhancing our understanding of its frictional behavior. The research is divided into two main components: simulation work and experimental investigations. The specific objectives include:

- Literature Review and Model Selection: From the existing friction models used in precision engineering systems, select an appropriate model for further investigation.
- Simulations: Develop a computational model of the Proton Motion Stage that incorporates the selected friction model. Simulate the behavior of the system to explore the effects of different parameters and gain insights into friction dynamics.
- Experimental Investigations: Perform a series of experiments on the Proton Motion Stage to identify friction parameters. This includes friction coefficients analysis and the study of position-dependent effects on friction forces.
- Comparison and Insights: Compare the findings from simulations and experimental investigations to have a deeper understanding of friction identification and friction behavior in the Proton Motion Stage.

1.3. Outline

The rest of the thesis is organized as follows:

- **Chapter 2**: This chapter presents a comprehensive review of existing friction models employed in precision engineering systems. The strengths and limitations of different models are discussed, leading to the selection of the LuGre friction model for further investigation.

- **Chapter 3**: In this chapter, the principle of the LuGre friction model and the identification of friction parameters are explained. A sensitivity analysis of these parameters is also conducted to explain identification results.
- **Chapter 4**: The focus of this chapter is on the experiments conducted on the Proton Motion Stage. In this chapter, first, the position-dependent cable-slab force is modeled. Then, the identification of static and dynamic parameters is conducted.
- **Chapter 5**: This chapter includes a summary of the key findings of the thesis and suggestions for future research and development in understanding of friction in the motion control system.

2

Literature Review

2.1. Static Friction Models

Friction, as a highly nonlinear natural phenomenon, presents a challenge in modeling, including when the velocity crosses zero. In an effort to characterize this complex behavior, friction models have been broadly classified into two categories: static and dynamic [3]. Static models predominantly involve a fixed mapping from velocity to force, while dynamic models consider not only this mapping but also the temporal relationship between these variables. This section will provide an overview of some of the static models [10].

2.1.1. Coulomb Friction

Coulomb friction is named after Charles-Augustin de Coulomb and is one of the oldest friction models [11]. The Coulomb friction model approximates friction force as zero at zero velocity, and a constant value at other non-zero velocities, with the direction opposite to the moving direction, as explained mathematically by

$$f = F_C \mathsf{sgn}(v), \tag{2.1}$$

where F_C is the Coulomb friction and v is the sliding velocity [10].

2.1.2. Viscous Friction

Since the emergence of hydrodynamics theory, Reynolds proposed that viscous friction in lubricated situations is proportional to velocity.

$$f = \sigma_{viscous} v, \tag{2.2}$$

where $\sigma_{viscous}$ is the viscous coefficient [10][3]. It is common to combine the Coulomb and viscous friction models, where the friction force at zero velocity is non-zero, as shown in Figure 2.1.

2.1.3. Stiction

The concept of stiction is introduced by Morin, defined as the force that must be overcome during the motion initialization [12]. Compared to the Coulomb friction model, the stiction at zero velocity is generally larger than the Coulomb friction. The most famous and commonly used in engineering is the combination of static, Coulomb and viscous friction models, because it preserves simplicity while satisfying industrial accuracy requirements, as illustrated in Figure 2.1(d) [2].

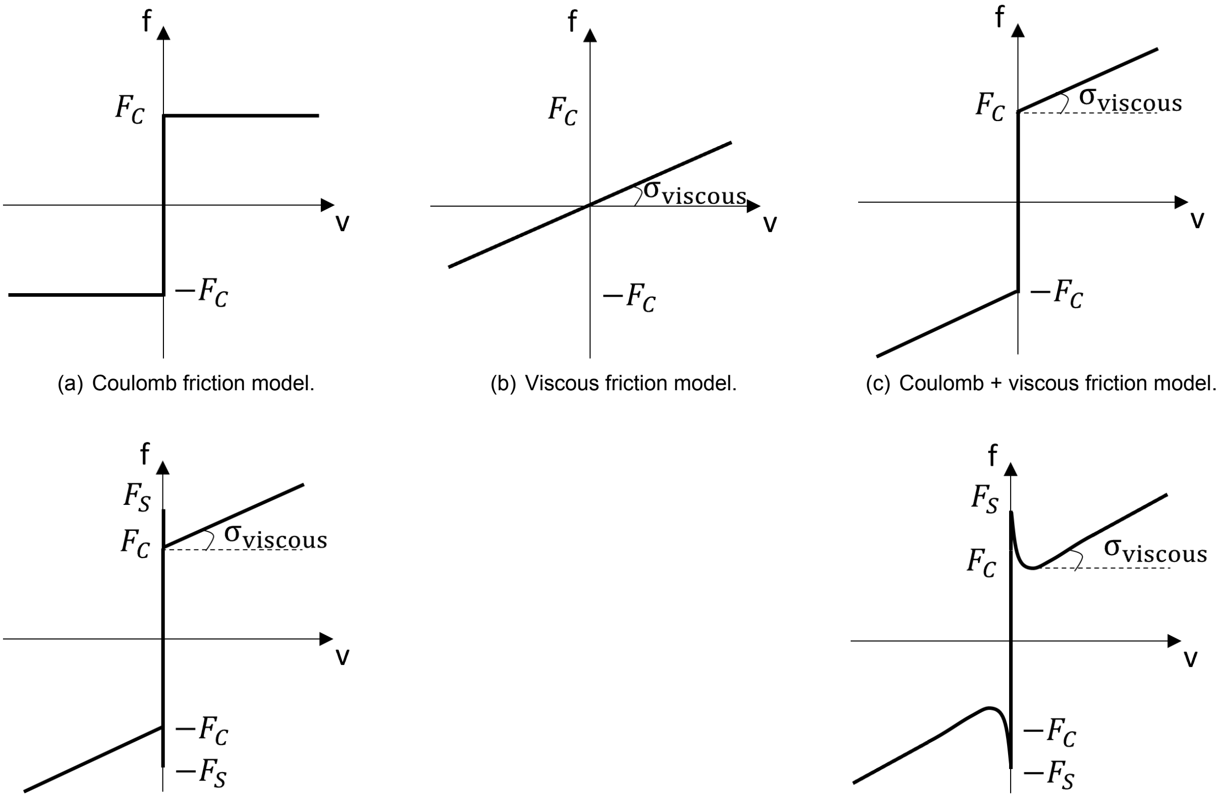

(a) Coulomb friction model.

(b) Viscous friction model.

(c) Coulomb + viscous friction model.

(d) Coulomb + viscous + stiction friction model.

(e) Stribeck effect + viscous. Tustin friction model.

Figure 2.1: Static friction models.

2.1.4. Stribeck Curve

The Stribeck curve models the friction force when the relative velocity between two contacting surfaces is non-zero from a stand-still state. In the Stribeck curve, four regimes are presented, including pre-sliding friction, boundary lubrication, partial fluid lubrication, and full fluid lubrication [3].

In the static friction regime, it is assumed that the velocity of relative movement is zero, but a small velocity exists when the contacting surfaces are deformed. The asperity of the contact surface is idealized as springs when the displacement is very small. Before the breakaway happens, the tangential force F_t applied on the spring-like asperity junction is:

$$F_t(x) = -k_t z, \tag{2.3}$$

where z is the displacement before the junction starts sliding, and k_t is the stiffness of the spring. The asperities deform in reaction to the tangential force and recover when the force is absent.

With the increase of the tangential force F_f, the displacement z reaches the maximum value z_{max}, the springs breakaway and the contacting surfaces start to slide, resulting in the relative velocity becoming larger than zero, as shown in 2.2

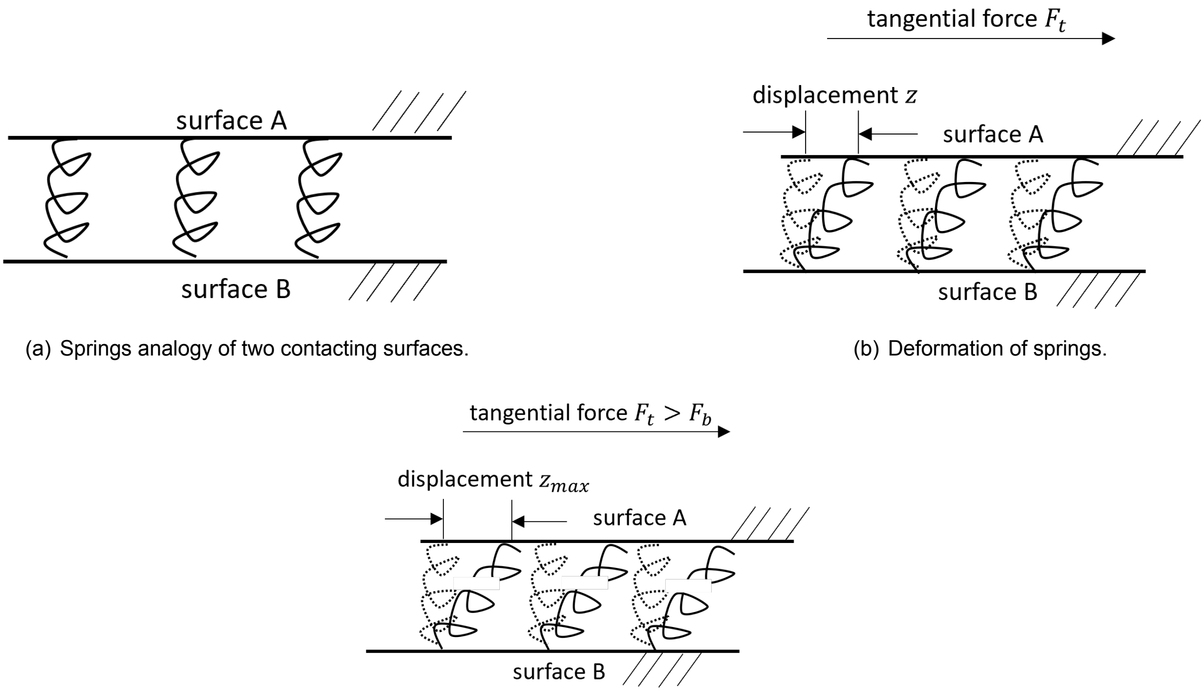

(a) Springs analogy of two contacting surfaces.

(b) Deformation of springs.

(c) Breakaway when displacement reaches the maximum value.

Figure 2.2: Regime 1: static friction.

In the second regime, the contact surfaces create some space between each other but the velocity is still not large enough to generate a lubrication film. Since this regime preserves the shearing action between two solid surfaces, the friction force in this regime is larger than the following regimes three and four [13].

The further velocity increase introduces a lubrication film into the contact surface in regime three, but the lubrication film is not thicker than the asperities. Therefore, solid contact still exists and results in partial fluid lubrication. As the velocity keeps increasing, the solid contact between two surfaces decreases, and the lubrication film increases, resulting in a smaller friction force and larger acceleration [14].

The lubrication film grows further with the sliding motion in the fourth regime, so the solid contact is eliminated and the contact surfaces are fully supported by fluid lubricants.

The microscopic analogies of the two contacting surfaces in regimes 2, 3, and 4 are shown in 2.3:

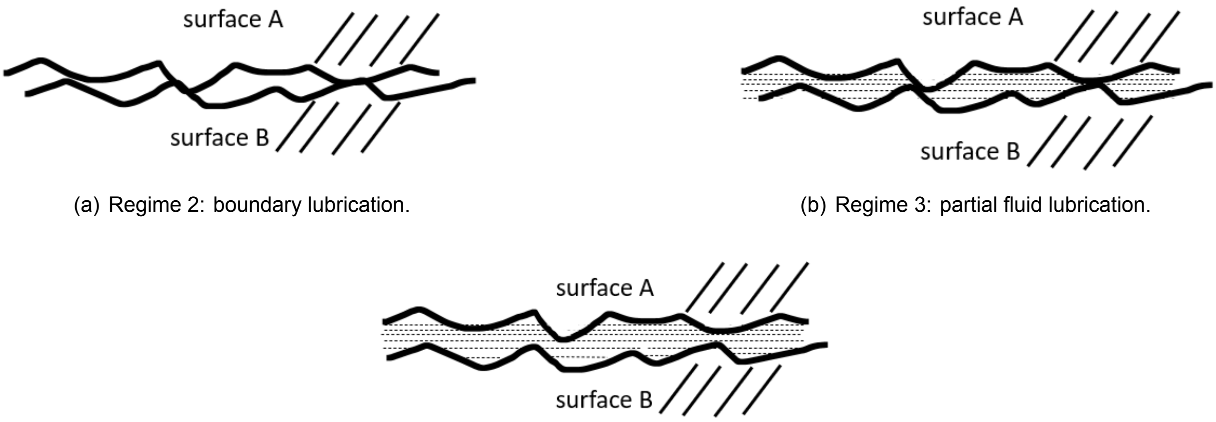

(a) Regime 2: boundary lubrication.

(b) Regime 3: partial fluid lubrication.

(c) Regime 4: full partial fluid lubrication.

Figure 2.3: Regime 2,3, and 4 in Stribeck curve.

The Stribeck curve shows how friction force changes with velocity in regimes 2,3 and 4, and the friction force in regime 1 does not change with velocity [15].

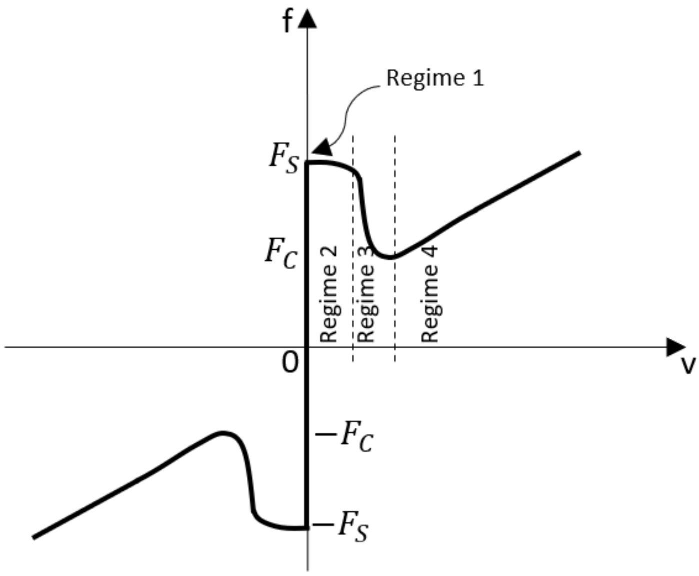

Figure 2.4: Generalized Stribeck curve.

The Tustin friction model [16]can be written as

$$f = \text{sign}(v)s(v) + \sigma_2 v, \tag{2.4}$$

where $s(v)$ is a continuous parameterized curve that represents the Stribeck effect, $\sigma_2 v$ is the viscous friction term, and the most common form of s is

$$s(v) = F_c + (F_s - F_c)e^{-(\frac{v}{v_0})^{\delta_s}}, \tag{2.5}$$

where δ_s is the Stribeck shape parameter, F_C is the Coulomb friction, F_S is the stiction friction, and v_0 is the velocity with respect to the Coulomb friction.

2.2. Dynamic Friction Models

The static models fail to explain the following:

- hysteresis behavior in the situation of non-stationary velocities;
- different experimental conditions including the variations of contact surfaces can result in various breakaway forces;
- in the sticking phase (regime 1), small displacements should also be considered.

Dynamic models mainly describe the spring-like behavior during the first regime (pre-sliding regime), including hysteresis behavior and varying break-away forces [5].

2.2.1. LuGre model

LuGre model integrates the Stribeck curve and the pre-sliding regime. The name of the LuGre model is the abbreviation of the Lund Institute of Technology and INPG Grenoble. As shown in Figure 2.5, the LuGre model adopts the analogy from the Dahl model [17] and compares the contact surfaces to two sides of bristles, where one side is considered rigid for simplicity [2].

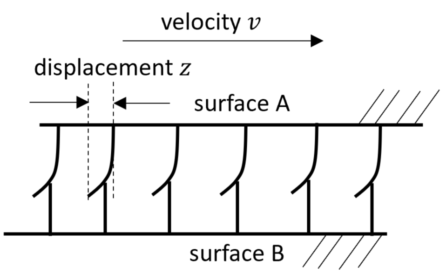

Figure 2.5: Bristles model to describe contact surface [5]

In the pre-sliding stage, the average deflection of the bristles z can be described as

$$\frac{dz}{dt} = v - \frac{\sigma_0|v|}{s(v)}z, \tag{2.6}$$

where v is the relative velocity of the sliding movement, and σ_0 represents the stiffness coefficient.

The deflection z generates friction force F by

$$F = \sigma_0 z + \sigma_1 \frac{dz}{dt} + \sigma_2 v, \tag{2.7}$$

in which σ_1 is the micro-viscous damping coefficient and σ_2 is the viscous damping coefficient.

With increasing of the displacement z, the change of displacement $\frac{dz}{dt}$ reaches zero, and z approaches the maximum value

$$z_{max} = \frac{vs(v)}{|v|\sigma_0} = \text{sign}\frac{s(v)}{\sigma_0}, \tag{2.8}$$

the friction force enters the steady-state stage, where z stays constant.

From Equation 2.5, 2.7 and 2.8, the friction force for steady-state can be described as

$$\begin{aligned} F_{ss}(v) &= s(v)\text{sign}(v) + \sigma_2 v \\ &= F_C\text{sign}(v) + (F_S - F_C)e^{-(\frac{v}{v_s})^2}\text{sign}(v) + \sigma_2 v. \end{aligned} \tag{2.9}$$

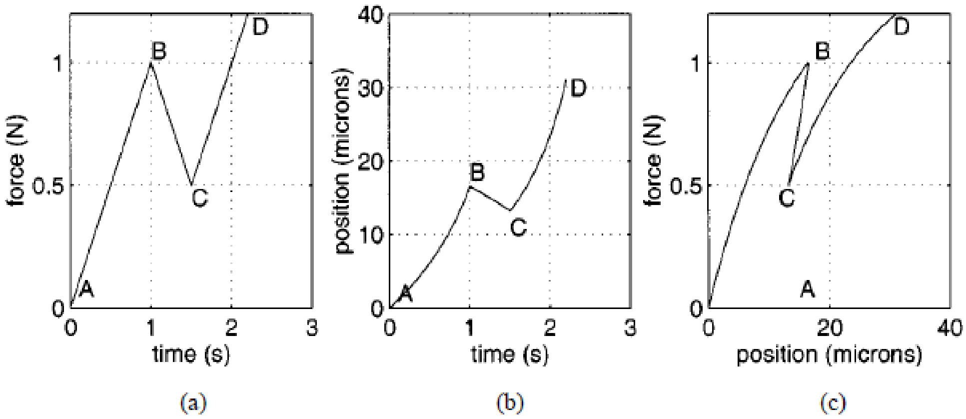

Figure 2.6: LuGre simulation results: (a) applied external force, (b) resulting position, (c) resulting position-force relationship.

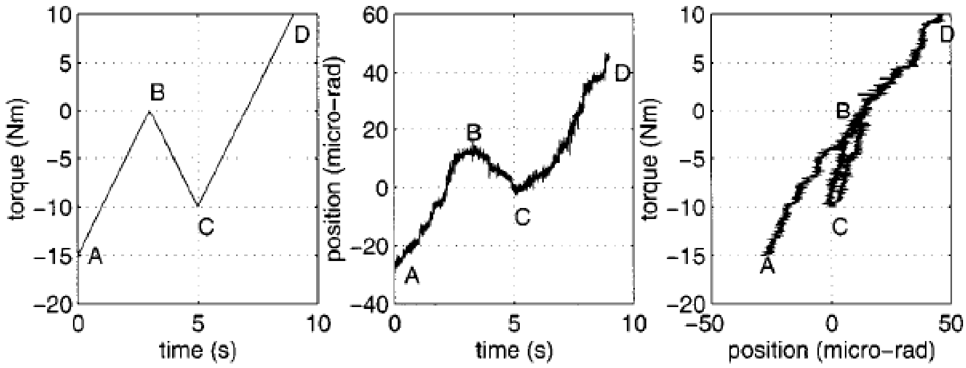

Figure 2.7: Experimental results: (a) applied torque, (b) resulting angular position, (c) resulting position-torque relationship.

As shown in Figure 2.6 and 2.7, the LuGre model fails to capture the internal loop in the position-force relation, which means it cannot cover the reversal point memory, also called nonlocal memory. By enabling the nonlocal memory, friction force can be calculated disregarding the number of velocity reversals [5].

2.2.2. Leuven model

The Leuven friction model builds upon the LuGre model to improve its accuracy in describing friction dynamics by introducing hysteresis behavior with nonlocal memory[6]. The Leuven model consists of two equations:

- The friction force equation:

$$F = F_h(z) + \sigma_1 \frac{dz}{dt} + \sigma_2 v, \tag{2.10}$$

- The nonlinear state equation:

$$\frac{dz}{dt} = v \left(1 - sign\left(\frac{F_d(z)}{s(v) - F_b}\right) \left|\frac{F_d(z)}{s(v) - F_b}\right|^n\right), \tag{2.11}$$

The parameters are listed below:

- $F_h(z)$: the hysteresis friction force, which is the part of the friction force that shows hysteresis behavior;

- n: the transition curve shape coefficient;
- $F_d(z)$: the transition curve of piecewise-linear spring characteristic of z that is active at a certain time;
- F_b: the beginning point of the curve.

To describe the pre-sliding stage, (2.10) is reduced to

$$F = F_b + F_d(z) = F_h(z)$$
$$\frac{dz}{dt} = 0 \tag{2.12}$$

because the velocity is zero.

Two stacks are required to implement $F_h(z)$: stack m for the minimum value of $F_h(z)$ in ascending order and stack M for the maximum value of $F_h(z)$ in descending order. These stacks grow at velocity reversals, shrink when internal hysteresis loops are closed.

During each time velocity reversal, if the transition curve is descending, the value of F_b is added to the current value of stack M, and if the transition curve is ascending, the value of F_b is added to the current value of stack m. In this way, when the velocity reversal finishes, the new extreme values of F_h would be added to stack M and m. When an internal loop, as shown in Figure 2.7 closes, the Leuven model wipes out the extreme values within the internal loop from the stacks, just like the loop has never happened. The stacks are reset when the stage shifts from pre-sliding to sliding.

With this procedure, the displacement z is reset to zero value when a velocity reversal is finished and recalculated when an internal loop is closed[6].

To describe the steady-state stage, $s(v) = F_d(z) + F_b$, and the friction is described similarly to Equation (3.5) in the LuGre model.

2.2.3. Modified Leuven model

Based on the Leuven model, there are two major modifications [7]:

- Adaptation of the state equation to overcome discontinuities.

  In the Leuven model, when an internal loop closes or starts, the values of z and $F_d(z)$ are re-set to zero and the value of F_b is set to $F_h(z)$. This leads to a discontinuity of the values of $F_h(z)$ and F_b, which causes the discontinuity of $F_d(z)/(s(v) - F_b)$ and eventually makes dz/dt discontinuous. This will ultimately lead to the friction force being discontinued since friction force is calculated from dz/dt.

  Modified Leuven method replaced $\frac{F_d(z)}{s(v)-F_b(z)}$ with $\frac{F_h}{s(v)}$, to avoid the discontinuity in the friction force brought by the sudden change of $F_d(z)$ and F_b.

$$\frac{dz}{dt} = v\left(1 - \text{sign}\left(\frac{F_h(z)}{s(v)}\right)\left|\frac{F_h(z)}{s(v)}\right|^n\right) \tag{2.13}$$

- Maxwell Slip implementation to overcome stack overflow.

  In the Leuven model, a potential implementation error can arise if the memory stacks become overwhelmed due to an excessive number of initiated loops. This situation can occur due to the necessity of predefining the stack size beforehand. Also, since the stack must be reset during the shift from the pre-sliding and sliding phase, a clear boundary between the two phases must be drawn. Therefore, the second major modification is the replacement of the hysteresis force function with the Maxwell Slip model [7].

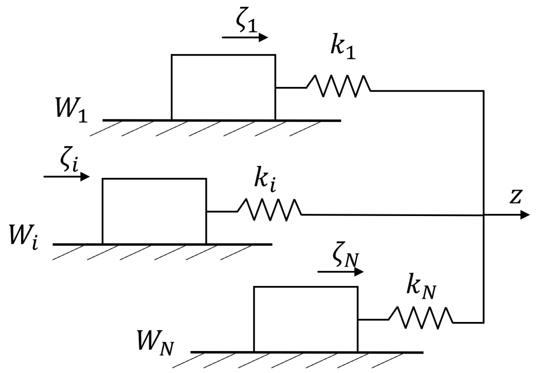

Figure 2.8: Maxwell Slip model for N elements

Modified Leuven method realizes hysteresis behavior by using N parallel Maxwell Slip elements with the same input of the displacement and the same output F_i. The hysteresis force F_h equals the sum of F_i. Each Maxwell-Slip element is described as:

$$\text{if } |z-\zeta_i| < \frac{F_{bi}}{k_i} \quad \text{then} \quad \begin{cases} F_i = k_i(z-\zeta_i) \\ \zeta_i = \text{const.} \end{cases}$$
$$\text{else} \quad \begin{cases} F_i = \text{sign}(z-\zeta_i)F_b i \\ \zeta_i = z - \text{sign}(z-\zeta_i)\dfrac{F_{bi}}{k_i}. \end{cases} \tag{2.14}$$

$$F_h = \sum_{i=1}^{N} F_i. \tag{2.15}$$

In the equation, the parameters' meanings are:

- F_{bi}: the maximum force,
- k_i: a linear spring constant,
- ζ_i the position of the element i.

The first part of the equation describes the sticking phase, and the second describes the slipping phase. The sum of hysteresis forces F_i equal the hysteresis force F_h [7].

2.2.4. Generalized Maxwell-Slip Model

The Generalized Maxwell Slip model (GMS) builds upon the modified Leuven model introduced in the previous section. In this advancement, the Maxwell slip model introduces a change to the hysteresis function used in the modified Leuven model. Specifically, the Coulomb law at the point of slip is replaced with a rate-state law. [8].

Similar to the Maxwell-Slip model, GMS can also be represented as N parallel connected elastoslide elements with the same input (v or z) and different sets of parameters. With the velocity input v and the z_i as the ith element of state vector **z**, for each elements the dynamics can be determined as:

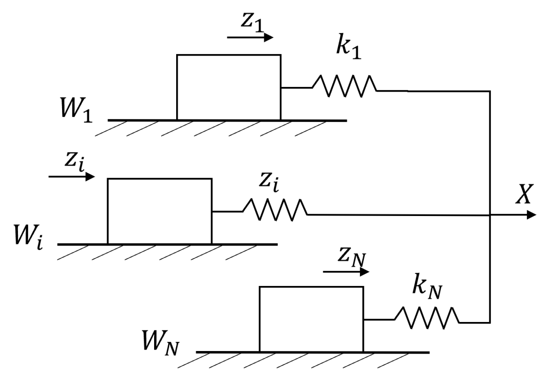

Figure 2.9: Maxwell Slip model for N massless elements.

- For the element i in the pre-sliding phase:

$$\frac{dz_i}{dt} = v \tag{2.16}$$

  and the pre-sliding phase remains until $z_i = s_i(v)$, where $s_i(v)$ is the Stribeck function for element i.

- For element i in the sliding phase:

$$\frac{dz_i}{dt} = \text{sign}(v)C_i\left(1 - \frac{z_i}{s_i(v)}\right), \tag{2.17}$$

  where C_i is the attraction parameter that determines the speed of convergence for z_i to s_i.
  The slipping phase remains until velocity reversal.

The friction force is the sum of the friction force output of the N elements and two extra terms for effects not included in the model.

$$F_f(t) = \sum_{i=1}^{N}(k_i z_i(t) + \sigma_i \dot{z}_i(t)) + f_v iscous(v), \tag{2.18}$$

in which the first term is the elastic-sliding friction force, the second is the viscoelastic behavior, and the last term is the viscous component proportional to velocity $v(t)$ [8].

2.3. A Comparison of Friction Models

In this chapter, friction models including static and dynamic friction models are introduced. For friction identification in later simulation and experiment work, one of the friction models is selected based on the criteria of

- Coverage of static friction phenomena;
- Coverage of dynamic friction phenomena;
- Accuracy;
- Easy to identify.

Among all the static models, the Tustin friction model explained the four regimes of the friction force most detail. However, the Tustin model failed to explain the displacement and the variations of breakaway force in the pre-sliding stage. Since the Proton Motion Stage can move in near zero velocities, the dynamic friction phenomena is an important research interest in this thesis work. The selection is limited to the dynamic friction models for the need of dynamic friction phenomena [2].

The LuGre model creates a unified model that applies to both the pre-sliding and sliding stages, as well as the transition between them. While the LuGre model can successfully encompass most of the known friction phenomena, it remains incapable of representing hysteresis with nonlocal memory and addressing undesired position drift observed in simulations [18].

The Leuven model resolves these problems, yet introduces numerical and implementation challenges. However, through two specific adjustments, the modified Leuven model successfully resolves the discontinuity and implementation issues. Thus, the modified Leuven model is chosen over the Leuven model. Furthermore, the model briefly touches on physics-based friction models, paving the way for the introduction of the Generalized Maxwell Slip model. However, due to the elaborateness and complexity, the ability to support fast simulation and calculation is limited. [8]

The GMS model employs multiple internal states z instead of just one, which enables an even more accurate description of pre-sliding behavior. However, an issue with the GMS model is the challenge of determining the precise number of internal states required to achieve an accurate identification of the friction force. To address this limitation, two potential solutions are under consideration:

- Set a fixed number of internal states;
- Adjust the number through the identification procedure, based on the identification performance.

For the first solution, the determination of the fixed number for all positions of the Proton Motion Stage is hard, as different positions fit the model differently. The second solution introduces high complexity to the identification procedure.

The decision between the LuGre model and the GMS model leads to the trade-off between identification complexity and the coverage of non-local memory [19]. Because the Proton Motion Stage runs mostly in the velocity belongs to the second, third, and fourth regimes, the coverage of non-local memory is considered less important than the identification complexity added by GMS. Based on the comparisons in Table 2.1, the LuGre model is selected for the model-based identification [20][21].

	coverage of static friction phenomena	coverage of dynamic friction phenomena	accuracy	easy to identify
Tustin model	+	-	- -	++
LuGre model	+	+	+/-	+
Leuven model	+	+	+	- -
Modified Leuven model	+	+	++	-
GMS model	+	+	++	- -

Table 2.1: A comparison of friction models.

3
Parameter Identification

3.1. Introduction

This chapter focuses on the simulation and parameter identification of the LuGre friction model. The LuGre model is a widely used friction model that describes the friction between two surfaces using a combination of elastic, viscous, and Coulomb friction forces, introduced in the previous chapter. This chapter will explain the identification problem, the methodology used, and the discussion based on the results. For the pre-sliding stage of the LuGre model, the hysteresis effect has to be captured during performing velocity reversals. For the steady state, the friction force at different velocities is required. So the parameter identification consists of two parts: static parameter identification for steady state and dynamic parameter identification for the pre-sliding stage. The static parameter identification constructs a velocity-friction map using constant non-zero velocities. Dynamic parameter identification is made by measuring velocity and friction while applying a motion profile with velocity reversals [22]. The optimization method implemented for both static and dynamic parameter identifications is the Levenberg–Marquardt algorithm [23]. Based on the simulation results, a discussion about the noise level dependency of the identification of parameters is also presented in this chapter.

3.2. LuGre Model and Parameters

The LuGre model[5] describes the stage of the internal dynamics between two touching surfaces before the relative sliding motion begins as the pre-sliding stage:

$$s(v) = F_C + (F_S - F_C)e^{-(\frac{v}{v_0})^{\delta_s}}, \tag{3.1}$$

$$\frac{dz}{dt} = v - \frac{\sigma_0|v|}{s(v)}z, \tag{3.2}$$

$$F = \sigma_0 z + \sigma_1\frac{dz}{dt} + \sigma_2 v, \tag{3.3}$$

$$z_{\text{max}} = \frac{vs(v)}{|v|\sigma_0} = \text{sign}(v)\frac{s(v)}{\sigma_0}, \tag{3.4}$$

in which the parameters

- F_S: the stiction force;
- F_C: the Coulomb force;
- v_0: the velocity when the friction is F_C;
- δ_s: the Stribeck shape parameter, set to 2 in this work [5];
- v: the relative velocity of the two contacting surfaces;
- F: the friction force between the two contacting surfaces;
- z: the relative displacement of the bristles, the analogy of the two surfaces in the LuGre model;
- z_{max}: the maximum displacement of the bristles, before the sliding happens;

- t: time;
- σ_0: the stiffness coefficient;
- σ_1: the micro-viscous damping coefficient;
- σ_2: the viscous damping coefficient.

The friction force enters the steady-state stage, where the friction force can be described as

$$\begin{aligned} F_{\text{ss}}(v) &= s(v)\text{sign}(v) + \sigma_2 v \\ &= F_C\text{sign}(v) + (F_S - F_C)e^{-(\frac{v}{v_0})^2}\text{sign}(v) + \sigma_2 v. \end{aligned} \tag{3.5}$$

In the pre-sliding stage, with the change of velocity, external force, and friction force, the bending of the bristles changes. Therefore, the pre-sliding stage is also called the dynamic stage. The parameters that characterize the LuGre model in the dynamic stage are σ_0 and σ_1, called dynamic parameters [22][24]

In the steady state, the displacement of the bristles already reaches its maximum value and stops changing, so the steady state is also called the static stage. The parameters that characterize the LuGre model in the static stage are σ_2, F_C, F_S, and v_0, called static parameters[25].

3.3. Methodology

3.3.1. Levenberg–Marquardt algorithm [26]

The identification problem is formulated as a least-squares optimization problem, with the cost function defined as the sum of the squares of the vector F, and the parameters to be identified formulated in the vector **x**.

The parameter vector **x** is defined as $\mathbf{x} = [x_1 \quad x_2 \quad \dots \quad x_n]^T$, where n is the number of parameters to be identified.

The vector of velocities collected from m timestamps is denoted as $\mathbf{v} = [v(t_1) \quad v(t_2) \quad \dots \quad v(t_m)]^T$.

The vector **F** is defined as $\mathbf{F}(\mathbf{x}, \mathbf{v}) = \begin{bmatrix} F_{\text{output}}(\mathbf{x}, v(t_1)) - F_{\text{measure}}(v(t_1)) \\ F_{\text{output}}(\mathbf{x}, v(t_2)) - F_{\text{measure}}(v(t_2)) \\ \vdots \\ F_{\text{output}}(\mathbf{x}, v(t_m)) - F_{\text{measure}}(v(t_m)) \end{bmatrix}$, where $F_{\text{output}}(\mathbf{x}, v(t_i))$ is the output friction force of velocity $v(t_i)$ using the parameters of the current iteration, and $F_{\text{measure}}(v(t_i))$ is the measured friction force of velocity $v(t_i)$.

The identification problem can be formulated as follows:

$$\min_{\mathbf{x}} c(\mathbf{x}), \tag{3.6}$$

$$where \quad c(\mathbf{x}) = \sum_{i=1}^{m} F^2(\mathbf{x}, v(t_i)) \tag{3.7}$$

$$= \sum_{i=1}^{m} (F_{\text{output}}(\mathbf{x}, v_i) - F_{\text{measure}}(v_i))^2, \tag{3.8}$$

The Levenberg–Marquardt algorithm finds the optimum solution iteratively. In each iteration k, the parameter vector $\mathbf{x}^{k+1}$ is updated by $\mathbf{x}^k + \mathbf{d}^k$, where $\mathbf{d}^k$ is the step size. So the objective function at the next iteration $\mathbf{x}^{k+1}$ be calculated as:

$$c(\mathbf{x}^k + \mathbf{d}^k, \mathbf{v}) = ||\mathbf{F}_{\text{output}}(\mathbf{x}^k + \mathbf{d}^k, \mathbf{v}) - \mathbf{F}_{\text{measure}}(\mathbf{v})||^2 \tag{3.9}$$

$$= [\mathbf{F}_{\text{output}}(\mathbf{x}^k + \mathbf{d}^k, \mathbf{v}) - \mathbf{F}_{\text{measure}}(\mathbf{v})]^T [\mathbf{F}_{\text{output}}(\mathbf{x}^k + \mathbf{d}^k, \mathbf{v}) - \mathbf{F}_{\text{measure}}(\mathbf{v})]. \tag{3.10}$$

To determine the optimal step size $\mathbf{d}^k$ of each iteration k, the derivative of $f(\mathbf{x}^k + \mathbf{d}^k)$ with respect to $\mathbf{d}^k$ is supposed to be set to zero, which is hard to perform analytically with Equation 3.10. Therefore, a series of successive linear approximations are used. $\mathbf{F}(\mathbf{x}^k + \mathbf{d}^k, \mathbf{v})$ can be linearized by

$$\mathbf{F}_{\text{output}}(\mathbf{x}^k + \mathbf{d}^k, \mathbf{v}) \approx \mathbf{F}_{\text{output}}(\mathbf{x}^k, \mathbf{v}) + \mathbf{J}(\mathbf{x}^k, \mathbf{v})\mathbf{d}^k, \tag{3.11}$$

where $\mathbf{J}(\mathbf{x}^k, \mathbf{v})$ is the Jacobian matrix of $\mathbf{F}(\mathbf{x}^k)$ with dimensions of $m \times n$, calculated by

$$\mathbf{J}(\mathbf{x}^k, \mathbf{v}) = \frac{\partial c(\mathbf{x}^k, \mathbf{v})}{\partial \mathbf{x}^k}. \tag{3.12}$$

With the linearization of Equation 3.11, Equation 3.10 can be further calculated by:

$$\begin{aligned}
c(\mathbf{x}^k + \mathbf{d}^k, \mathbf{v}) =& [\mathbf{F}_{\text{output}}(\mathbf{x}^k + \mathbf{d}^k, \mathbf{v}) - \mathbf{F}_{\text{measure}}(\mathbf{v})]^T [\mathbf{F}_{\text{output}}(\mathbf{x}^k + \mathbf{d}^k, \mathbf{v}) - \mathbf{F}_{\text{measure}}(\mathbf{v})] \\
\approx& [\mathbf{F}_{\text{output}}(\mathbf{x}^k, \mathbf{v}) + \mathbf{J}(\mathbf{x}^k, \mathbf{v})\mathbf{d}^k - \mathbf{F}_{\text{measure}}(\mathbf{v})]^T [\mathbf{F}_{\text{output}}(\mathbf{x}^k, \mathbf{v}) + \mathbf{J}(\mathbf{x}^k, \mathbf{v})\mathbf{d}^k - \mathbf{F}_{\text{measure}}(\mathbf{v})] \\
=& [\mathbf{F}_{\text{output}}(\mathbf{x}^k, \mathbf{v}) - \mathbf{F}_{\text{measure}}(\mathbf{v})]^T [\mathbf{F}_{\text{output}}(\mathbf{x}^k, \mathbf{v}) - \mathbf{F}_{\text{measure}}(\mathbf{v})] \\
&+ [\mathbf{F}_{\text{output}}(\mathbf{x}^k, \mathbf{v}) - \mathbf{F}_{\text{measure}}(\mathbf{v})]^T \mathbf{J}(\mathbf{x}^k, \mathbf{v})\mathbf{d}^k \\
&+ (\mathbf{J}(\mathbf{x}^k, \mathbf{v})\mathbf{d}^k)^T [\mathbf{F}_{\text{output}}(\mathbf{x}^k, \mathbf{v}) - \mathbf{F}_{\text{measure}}(\mathbf{v})] + (\mathbf{d}^k)^T \mathbf{J}^T(\mathbf{x}^k, \mathbf{v})\mathbf{J}(\mathbf{x}^k, \mathbf{v})\mathbf{d}^k \\
=& [\mathbf{F}_{\text{output}}(\mathbf{x}^k, \mathbf{v}) - \mathbf{F}_{\text{measure}}(\mathbf{v})]^T [\mathbf{F}_{\text{output}}(\mathbf{x}^k, \mathbf{v}) - \mathbf{F}_{\text{measure}}(\mathbf{v})] \\
&+ 2[\mathbf{F}_{\text{output}}(\mathbf{x}^k, \mathbf{v}) - \mathbf{F}_{\text{measure}}(\mathbf{v})]^T \mathbf{J}(\mathbf{x}^k, \mathbf{v})\mathbf{d}^k + (\mathbf{d}^k)^T \mathbf{J}^T(\mathbf{x}^k, \mathbf{v})\mathbf{J}(\mathbf{x}^k, \mathbf{v})\mathbf{d}^k.
\end{aligned} \tag{3.13}$$

In order to obtain the step size that minimizes the objective function the best, taking the derivative of $c(\mathbf{x}^k + \mathbf{d}^k, \mathbf{v})$ with respect to $\mathbf{d}^k$ and setting the derivative to zero yields the equation:

$$\mathbf{J}^T(\mathbf{x}^k, \mathbf{v})\mathbf{J}(\mathbf{x}^k, \mathbf{v})\mathbf{d}^k = -\mathbf{J}^T(\mathbf{x}^k, \mathbf{v})[\mathbf{F}_{\text{output}}(\mathbf{x}^k, \mathbf{v}) - \mathbf{F}_{\text{measure}}(\mathbf{v})], \tag{3.14}$$

so $\mathbf{d}^k$ is calculated:

$$\mathbf{d}^k = -(\mathbf{J}^T(\mathbf{x}^k, \mathbf{v})\mathbf{J}(\mathbf{x}^k, \mathbf{v}))^{-1}\mathbf{J}^T(\mathbf{x}^k, \mathbf{v})[\mathbf{F}_{\text{output}}(\mathbf{x}^k, \mathbf{v}) - \mathbf{F}_{\text{measure}}(\mathbf{v})], \tag{3.15}$$

which is the search direction of the Gauss-Newton method.

When the current step is far away from the optimum, the value of d^k is large since $\mathbf{F}_{\text{output}}(\mathbf{x}^k, \mathbf{v}) - \mathbf{F}_{\text{measure}}(\mathbf{v})$ is large. Therefore, the Gauss-Newton method updates parameters with big search steps for the next iteration, which causes the method to become unstable. The Levenberg-Marquardt method improves the Gauss-Newton method for this shortcoming by adding a damping term

$$(\mathbf{J}^T(\mathbf{x}^k, \mathbf{v})\mathbf{J}(\mathbf{x}^k, \mathbf{v}) + \lambda^k \mathbf{I})\mathbf{d}^k = -\mathbf{J}^T(\mathbf{x}^k, \mathbf{v})\mathbf{F}(\mathbf{x}^k, \mathbf{v}), \tag{3.16}$$

where $\mathbf{I}$ is the identity matrix, and the damping factor λ^k is adjusted as the iterations proceed. If $||\mathbf{F}(\mathbf{x}^k + \mathbf{d}^k)|| < ||\mathbf{F}(\mathbf{x}^k)||$, indicating a successful step, the $k+1$th point is closer to the optimal point, λ_{k+1} is set to 0.1 times λ_k to make larger search steps. On the other hand, if $||\mathbf{F}(\mathbf{x}^k + \mathbf{d}^k)|| \geq ||\mathbf{F}(\mathbf{x}^k)||$, indicating an unsuccessful step, then the value of $\mathbf{x}^{k+1}$ is discarded, and $\mathbf{x}^{k+1}$ takes the value of previous parameter vector $\mathbf{x}^k$. λ^{k+1} is set to 10 times the value of λ_k in order to make smaller and more careful search [27]. The iteration terminates when the objective function $c(\mathbf{x}^k, \mathbf{v})$ or step size $\mathbf{d}^k$ is smaller than the tolerance value. So in this way, the Levenberg-Marquardt method increases the stability while preserving the speed of convergence.

3.3.2. Static Parameter Identification

The static parameters to be identified are the viscous damping coefficient σ_2, the Coulomb friction F_C, the static friction F_S, and the Stribeck velocity v_0.

Velocity-friction maps are constructed in the simulation work to identify these static parameters. For positive velocity values, 50 velocity-friction data points are measured, ranging from 0.001 to 0.41 m/s. The negative velocity data is symmetrical to the positive velocities. Because the velocity reversal between positive and negative includes near-zero velocities that are not described by steady-state Equation 3.5, but in dynamic Equation 3.3, the identification process is performed separately for positive and negative velocities, and the final identification result is obtained as the average of the results from positive and negative velocities [22].

To initiate the identification process as close to the real values as possible, initial guesses for positive velocities are set as follows:

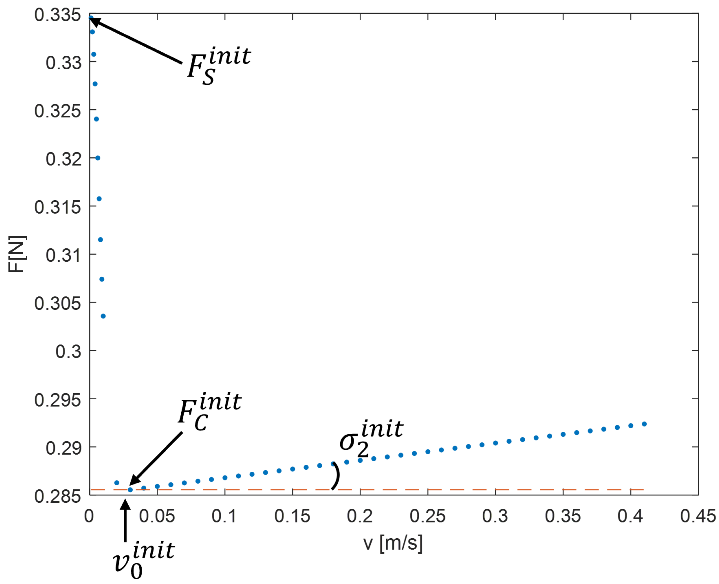

Figure 3.1: Initial guesses of static parameters on velocity-friction map.

- F_C^{init} is set to the minimum measured friction force $\min(F_{\text{measure}}(v))$, because the minimum friction force is Coulomb friction if no noise is presented [3]
- F_S^{init} is set as the friction force at the minimum velocity $F_{\text{measure}}(v(t_1))$. Since the friction force with respect to the minimum velocity is defined as static friction[3].
- v_0^{init} is determined by the velocity corresponding to the minimum friction force $\text{argmin}_v F_{\text{measure}}$.
- σ_2^{init} is calculated as the slope of the line between the point of minimum friction force and the friction force with the largest velocity on the velocity-friction map. Written in equation form is:

$$\sigma_2^{\text{init}} = \frac{F_{\text{measure}}(v(t_{\text{end}})) - \min(F_{\text{measure}}(v))}{v(t_{\text{end}}) - \text{argmin}_v F_{\text{measure}}}. \tag{3.17}$$

For negative velocities, the initial guesses are taken likewise.

3.3.3. Dynamic Parameter Identification

The dynamic parameters to be identified are the stiffness coefficient σ_0 and the micro-viscous coefficient σ_1. The initial guesses of the dynamic parameters are as follows:

- The initial guess of parameter σ_0 is calculated from Equation 3.5 and Equation 3.3. At the moment of the transition from the pre-sliding stage and the steady-state stage, the velocity is positive but has a value of near zero. The deflection z reaches the maximum distance and $\frac{dz}{dt}$ becomes almost zero. So Equation 3.5 and Equation 3.3 can be written as

$$F = \sigma_0 \max(z) \tag{3.18}$$

$$= F_c + F_S - F_C \tag{3.19}$$

where we set $\sigma_0^{\text{init}} = \frac{F_S}{\max(z)}$.

- The initial guess of σ_1 is set to a random value between 0 and σ_0^{init} [28].

3.4. Simulation Results

3.4.1. Input

The velocity input is generated by using the Prodrive Motion Platform trajectory generator.

For static parameter identification, velocities are obtained by setting initial and target positions as 0 and 0.2m, and gradually increasing the maximum velocity and a sampling rate of 10$^4/s. A step size of 0.01m/s is used from -0.41 to -0.01 and from 0.01 to 0.41m/s, and the step size is reduced to 0.001m/s in the interval of [-0.01m/s, -0.001m/s][0.001m/$ to F_C, as shown in Figure 3.3(a).

For example, for the maximum velocity of 0.001m/s, when moving from position 0 to 0.2m, the velocity changes with the sampling count in the following way:

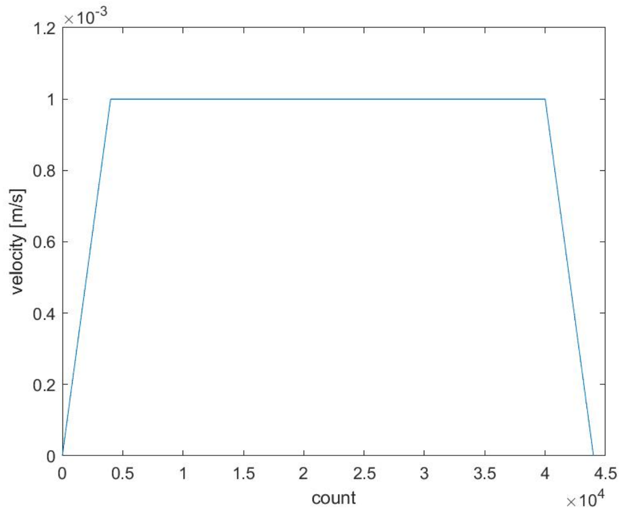

Figure 3.2: Velocity vs time with maximum velocity set to 0.001m/s.

With each maximum velocity, the friction force is collected by averaging the friction forces at the velocities that are at the flat plateau in the time-velocity relationship.

For dynamic parameter identification, the velocity input is constructed by having the carriage move back and forth from position -0.00005m to 0.00005m to realize repeated velocity reversals near the zero point, in order to simulate the pre-sliding stage of friction force.

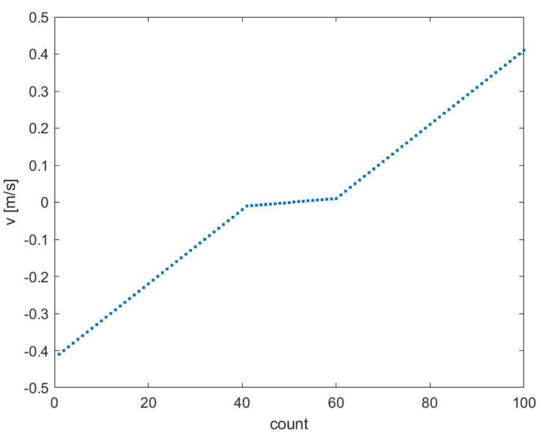

(a) Velocities for static parameter identification.

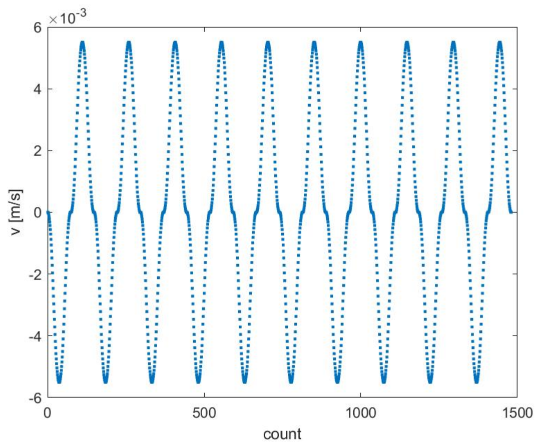

(b) The velocity inputs for static and dynamic parameter identification.

Figure 3.3: The velocity inputs for static and dynamic parameter identification.

In the simulation work, the measured friction forces corresponding to input velocities are calculated by using the LuGre friction model and adding Gaussian white noise with a signal-to-noise ratio of 80dB to the true values of friction forces.

3.4.2. Identification

Implementing the Levenberg–Marquardt(LM) method for parameter identification, the results are as follows. The tolerance of each component of search direction $\mathbf{d}^k$ is set to 1e-14 for static parameter identification, and 1e-6 for dynamic parameter identification. The iteration terminates when one of the components of $\mathbf{d}^k$ is smaller than the tolerant.

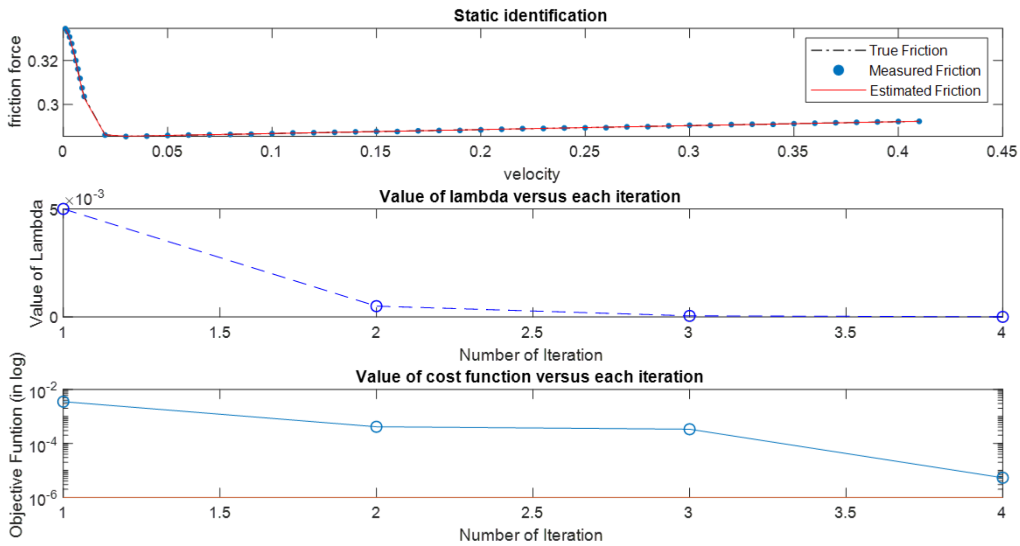

(a) Static parameter identification at positive velocities using LM method. The plot with negative velocities is identical.

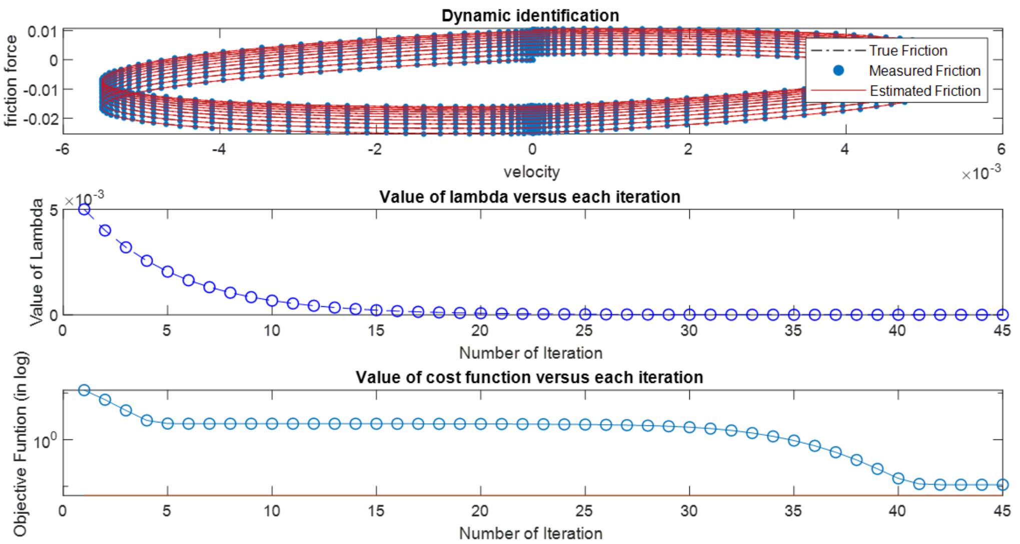

(b) Dynamic parameter identification using LM method.

Figure 3.4: LM method simulation.

After running 100 Monte-Carlo trials where in each trial the true friction is added with a white Gaussian noise with an SNR of 80dB, and taking the averages of the outputs, the identification results are shown below:

Friction Parameter	v>0	v<0	Nominal Value	True Value
F_C	0.2850	0.2850	0.2850	0.2850
F_S	0.3350	0.3350	0.3350	0.3350
v_0	0.0100	0.0100	0.0100	0.0100
σ_2	0.0179	0.0179	0.0179	0.0180
σ_0	–	–	259.9927	260
σ_1	–	–	0.6001	0.6000

Table 3.1: True value and simulation results.

The results show that it is obvious that the six parameters are identified with higher than 99% accuracy, and the errors are within an acceptable range.

3.4.3. Parameter sensitivity

Due to the presence of noise in the friction input, the locations of the global optimum for each parameter vary to different extents.

The error rate of a parameter p is defined as:

$$E(p) = \frac{\hat{p} - p}{p}, \tag{3.20}$$

where $\hat{p}$ is the estimated value of parameter p, and p is the true value.

When there is no noise added to the friction force, only alter the value of one parameter when the other five parameters are set to the true value, the objective function changes as follows:

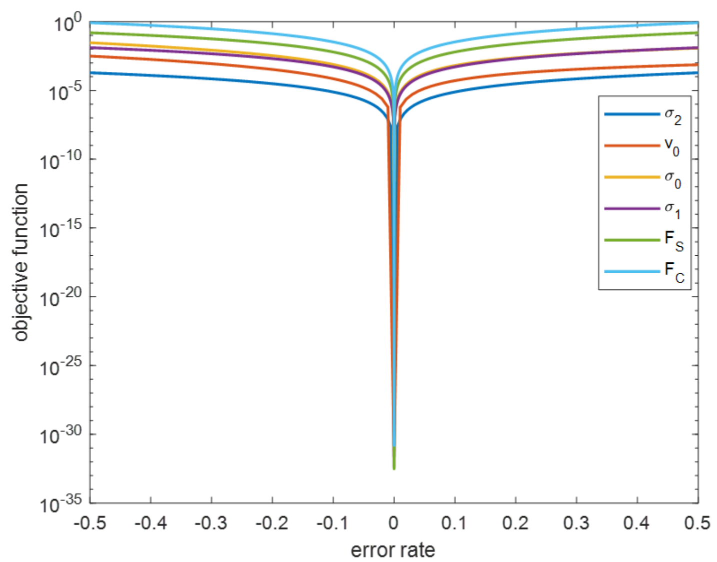

Figure 3.5: Sensitivity of objective function to changes of static and dynamic parameters.

From Figure 3.5, it is shown that when the error rate is zero, the objective function is zero as it means the most accurate estimation. With the change in the error rate of each parameter, the objective function responds differently. For example, at the same error rate, for the parameter F_C, the objective function is higher than other parameters, and for the parameter σ_2, the objective function is lower than other parameters. In this way, the objective function is more sensitive to the changes of F_C, and less sensitive to the changes of σ_2. This analysis leads to the explanation of the difference in identification results between each parameter.

After running 100 Monte-Carlo trails where each trial the true friction is added with a white Gaussian noise with an SNR of 80, the error rates of parameters are displayed as follows:

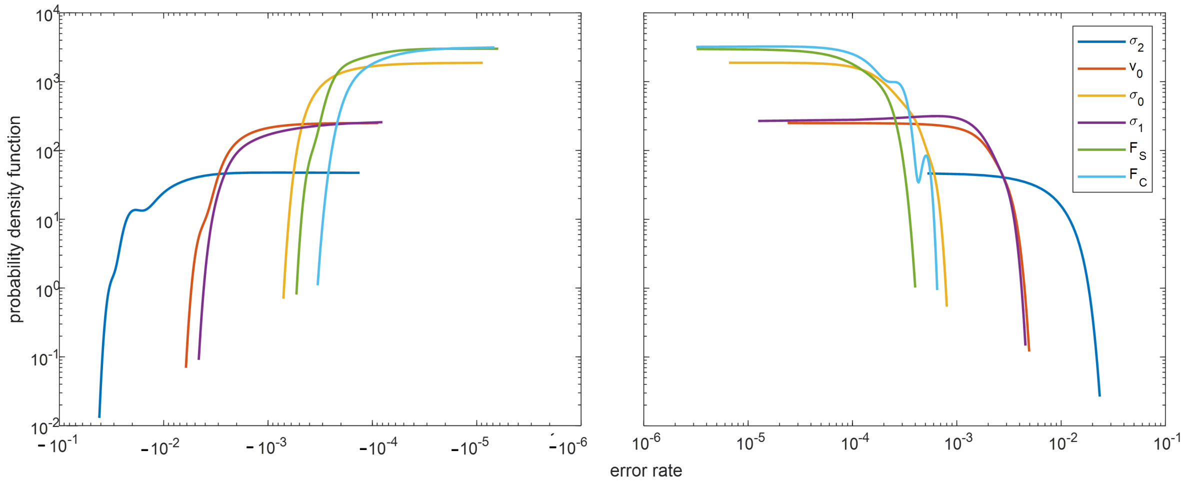

Figure 3.6: Probability density function of parameters from 100 Monte-Carlo trails.

Figure 3.6 illustrates the distributions of different parameter identification results. The static parameters F_C, F_S, v_0, and σ_1 have results that are centered around the true values with small variances. This indicates that the identification of these parameters is more accurate and less sensitive to the addition of noise to the friction force. On the other hand, the dynamic parameters, σ_2, show larger variances, with σ_1 slightly being overestimated compared to the true value.

This result coincides with Figure 3.5, where the objective function has the lowest sensitivity to the change of σ_2, and the sensitivity to v_0 and σ_1 is worse than F_C and F_S. This suggests that identifying these parameters is more susceptible to the effects of friction noise and may have less confidence.

3.5. Summary

This chapter focused on the simulation and parameter identification of the LuGre friction model, encompassing both static and dynamic parameter identification processes. Static parameter identification involved constructing velocity-friction maps and utilizing initial parameter guesses, while dynamic parameter identification simulated the pre-sliding stage with appropriate initial values. The Levenberg–Marquardt (LM) algorithm is used as the primary optimization method. Simulation results demonstrated the LM algorithm's effectiveness, achieving highly accurate parameter identification in the presence of noise. Sensitivity analysis revealed variations in parameter sensitivity, with some parameters exhibiting smaller variances. In summary, this chapter successfully addressed LuGre model parameter identification, shedding light on parameter sensitivity, which is crucial for modeling and controlling systems involving friction.

This chapter has laid the theoretical groundwork for identifying friction force. In the next chapter, practical experimentation will be conducted, where the theoretical knowledge is put to the test. Chapter 4 will introduce the Proton Motion Stage and the experiments to identify static and dynamic parameters. The feasibility of the identification approach presented in Chapter 3 will be discussed.

4 Experiments

4.1. Experiment Setup

The experiments are conducted on the Proton Motion Stage built by Prodrive Technologies. The Proton Motion Stage is a demonstrator of the motion control of a wafer inspection machine. It is a high-precision motion stage that consists of a vacuum-compatible XY gantry stage and a vibration isolation system. The performances of the Proton Motion Stage can be monitored with the software PMP (Prodrive Motion Platform). MatLab can be used to interact with the PMP systems, and code commands for the Proton Motion Stage.

Figure 4.1: Proton Motion Stage from Prodrive Technologies.

In this experiment work, the static and dynamic friction forces on the X-axis are studied. The relevant forces include inertia, friction force, and cable slab force, which can be described as:

$$f + F_{actuator} + F_{cable} = m * a, \tag{4.1}$$

where f is the friction force, $F_{actuator}$ is the actuator force applied to maintain the movements of the carrier, F_{cable} is the force introduced by the cable slab, m and a are the mass and acceleration of the carrier.

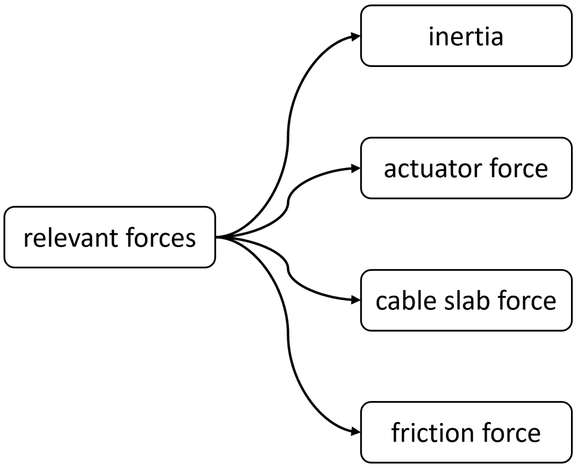

Figure 4.2: Relevant forces.

In the Proton Motion Stage, the actuator force is estimated from the current acting on the actuator with a proportional relation:

$$F_{actuator} = 53.4 * I_{actuator}, \tag{4.2}$$

where $I_{actuator}$ is the current.

4.2. Identification of Cable Slab Force

As shown in Figure 4.1, on the Proton Motion Stage, cable slabs are used to transmit power and information. However, the cable slabs also introduce a position-dependent force to the carrier. The cable slab force has a force on the carrier whether when it is moving to the positive or negative direction. Since this experiment aims to model the dynamic and static friction forces in different positions, the cable slab forces are not negligible.

To identify the cable slab forces, for simplicity, the acceleration in Equation 4.1 is set to zero, which means the carrier is controlled to move in constant velocities. At a certain position $position_i$, when the carrier is moving in the positive direction with the velocity v_p, Equation 4.1 can be written as:

$$f_p + F_{actuator,p} + F_{cable} = 0, \tag{4.3}$$

where the subscript p means positive direction, and n means negative direction.

When the carrier is moving in the negative direction with the velocity v_n, Equation 4.1 can be written as:

$$f_n + F_{actuator,n} + F_{cable} = 0. \tag{4.4}$$

The identification of cable slab force is based on the assumption that the velocities have the same value but opposite direction, the friction force also has the same value but opposite direction. So when $v_p = v_n$,

$$f_p + f_n = 0. \tag{4.5}$$

Adding Equation 4.3 and Euqation 4.4, the cable slab force at the $position_i$ is obtained as

$$F_{cable} = -(F_{actuator,p} + F_{actuator,n})/2. \tag{4.6}$$

On the Proton Motion Stage, first, the carrier is controlled to move with the velocity $v_p = 0.1$m/s from the position -0.15m to 0.15m with a sampling period of 0.0001 seconds. The movement is repeated 10 times. The actuator force at each sampling time is estimated from the actuator current, and the mean actuator force at the sampled position is calculated with the data from the 10 times movement.

Then, the carrier is controlled to move to the negative direction with the velocity $v_n = -0.1$m/s from the position 0.15m to -0.15m for 10 times. The range of movement and the sampling period are kept the same as in the positive direction movement. The actuator force is also estimated from the negative actuator current, and the mean actuator force is also calculated.

Finally, using (4.6), the cable slab force is calculated from the mean actuator force when moving in positive and negative directions.

The actuator forces and cable slab force in the experiment are smoothened with a Gaussian-weighted moving average filter in Matlab function `smoothdata` and are shown below:

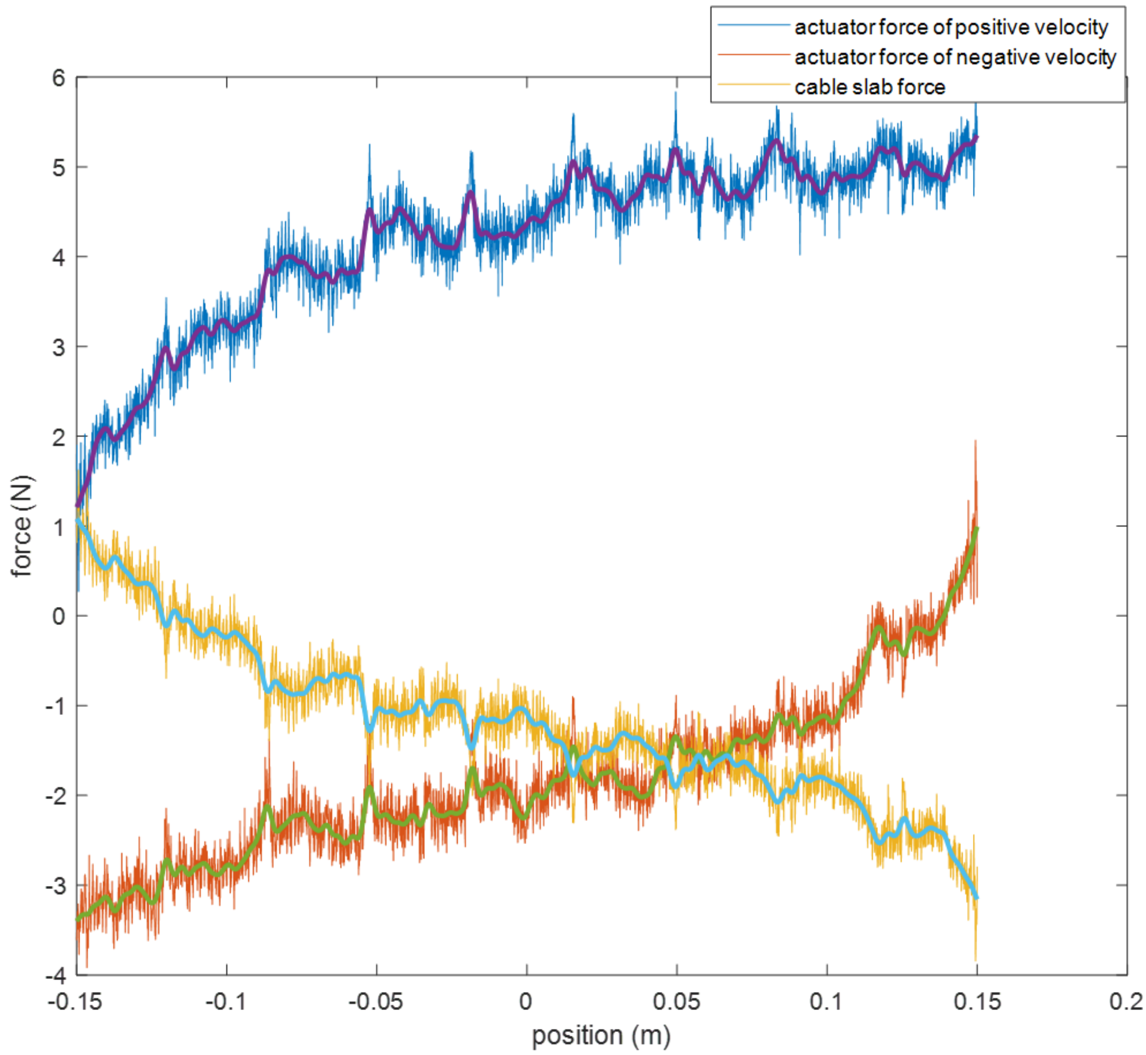

Figure 4.3: Cable slab force at position range [-0.15m,0.15m].

In Figure 4.3, the blue line and the red line are the actuator forces when moving in the positive and negative direction, respectively. The yellow line is the cable slab force at different positions.

From Figure 4.3, it is clear that as the position increases in the positive direction, the cable slab force increases in the negative direction. This matches the physical characteristic of the cable slab in Figure 4.1. The indication of the cable and the carrier is shown in Figure Figure 4.4. Figure 4.4(a) shows the carrier at position 1, and Figure 4.4(b) shows the carrier moved in a positive direction to position 2. From position 1 to position 2, the radius of folding of the cable slab increases, so there is less elastic energy stored in the cable slab, and thus more kinetic energy to drag the carrier. Therefore, the more the carrier moves in the positive direction, the more the cable slab force increases in the negative direction.

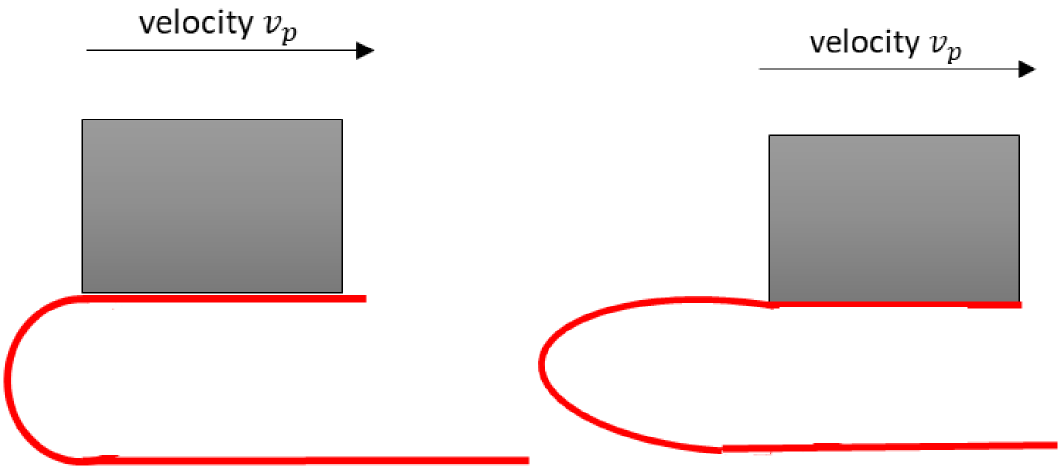

(a) Cable slab and carrier at position 1.

(b) Cable slab and carrier moved to the position direction to position 2.

Figure 4.4: Indication of cable slab and carrier. The cable slab is shown as red lines, and the carrier is shown as the blocks.

Moreover, in the curves of positive and negative actuator forces, the force spikes are evident in Figure 4.3. The spikes appear regularly every 0.034m, which is exactly the distance of the bearing rollers. Therefore, when investigating the friction forces at different positions, the spike areas should not be considered.

4.3. Static parameter experiments

4.3.1. Velocity-Friction Map

The identification of static parameters is conducted based on velocity-friction maps at various positions.

In the experiment, the carrier is controlled to move 0.005 meters with different constant velocities ranging from 0.001m/s to 0.25m/s by a closed-loop control system, where the actuator force applied in order to maintain the constant velocity is the control output. The output of the closed-loop system is the actuator force that is required for maintaining constant velocities. During the movements, the control output is sampled every 0.001 seconds. At each sampling point, the friction force is calculated in the same manner as Equation 4.3 and 4.4 by adding the sampled control output and the cable slab force obtained from Figure 4.3. To avoid the impact of the transition period, which is the period when the velocity changes from zero to the desired constant velocity, the carrier is controlled to move twice the effective distance, and only the latter half is considered, as explained in Figure 4.5.

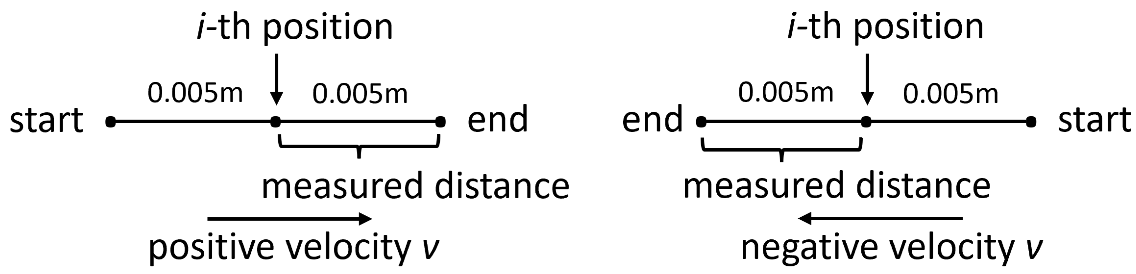

(a) Positive direction movement.

(b) Negative direction movement.

Figure 4.5: To avoid the impact of the transition period, the carrier is controlled to move twice the effective distance, and only the latter half is considered effective.

In order to better capture the Stribeck effect, the step size of increasing the velocity is 0.0001 between the velocity 0.0001 to 0.001, and 0.001 between the velocity 0.001m/s to 0.015m/s and increases to 0.01 when the velocity is up to 0.13m/s. The friction force of the i-th position with the velocity v is calculated by averaging the calculated friction force at sampling points in the effective distance.

The experiment is performed at 9 different positions on the x-axis. The position on the far left is -0.136m, where the velocity-friction force map is obtained as follows:

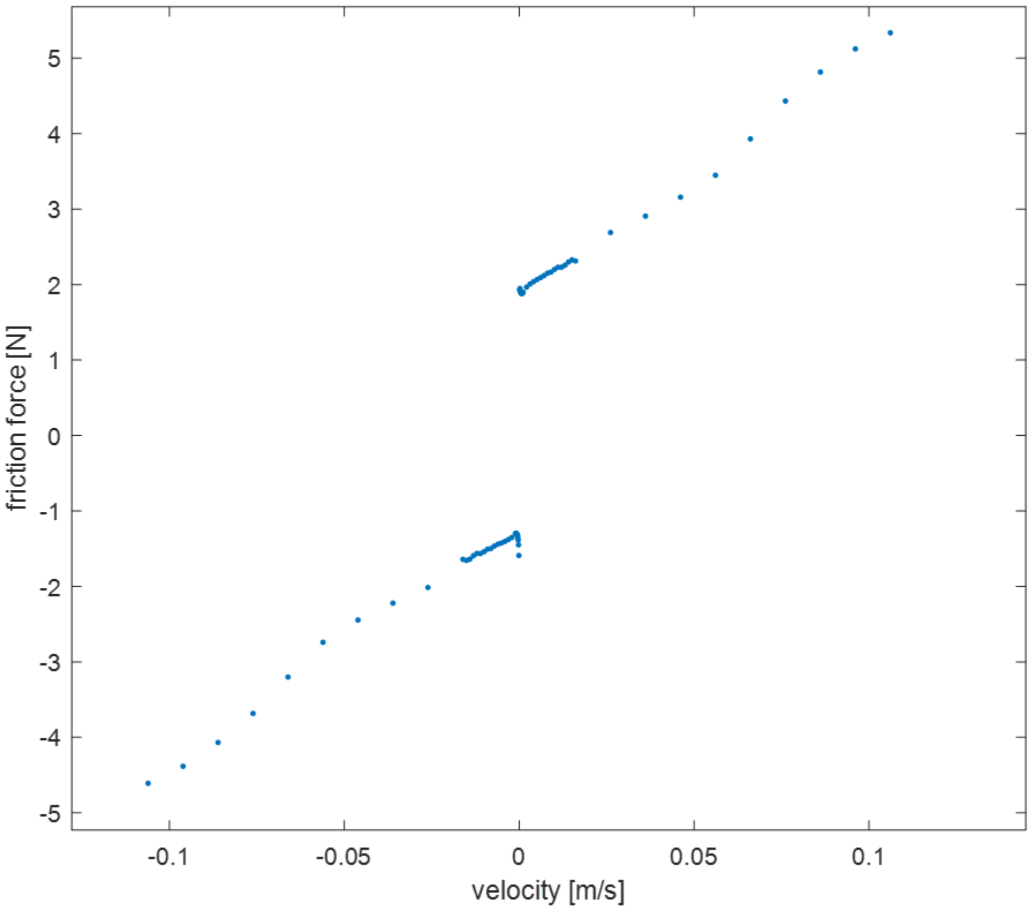

Figure 4.6: Velocity-friction map for static parameter identification at position -0.136m.

In Figure 4.6, at velocities far from zero, the friction forces with positive and negative velocities have a symmetrical increasing rate. At velocities near zero, the Stribeck effect is evident. For negative velocities, Columb friction force and Stribeck force are smaller than positive velocities.

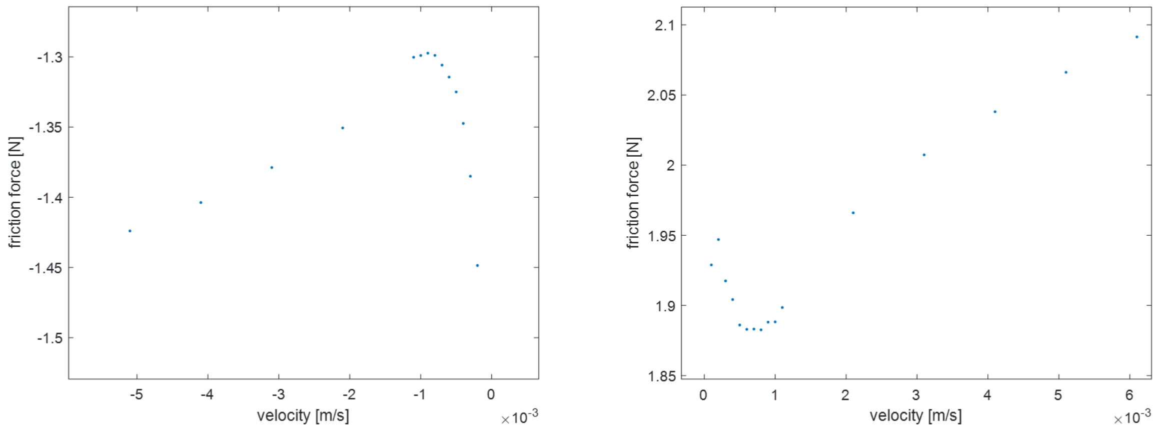

(a) Stribeck effect at negative velocity.

(b) Stribeck effect at positive velocity.

Figure 4.7: Stribeck effect at position -0.136m.

The velocity-friction force map is also obtained at various positions selected away from the spike areas shown in Figure 4.3.

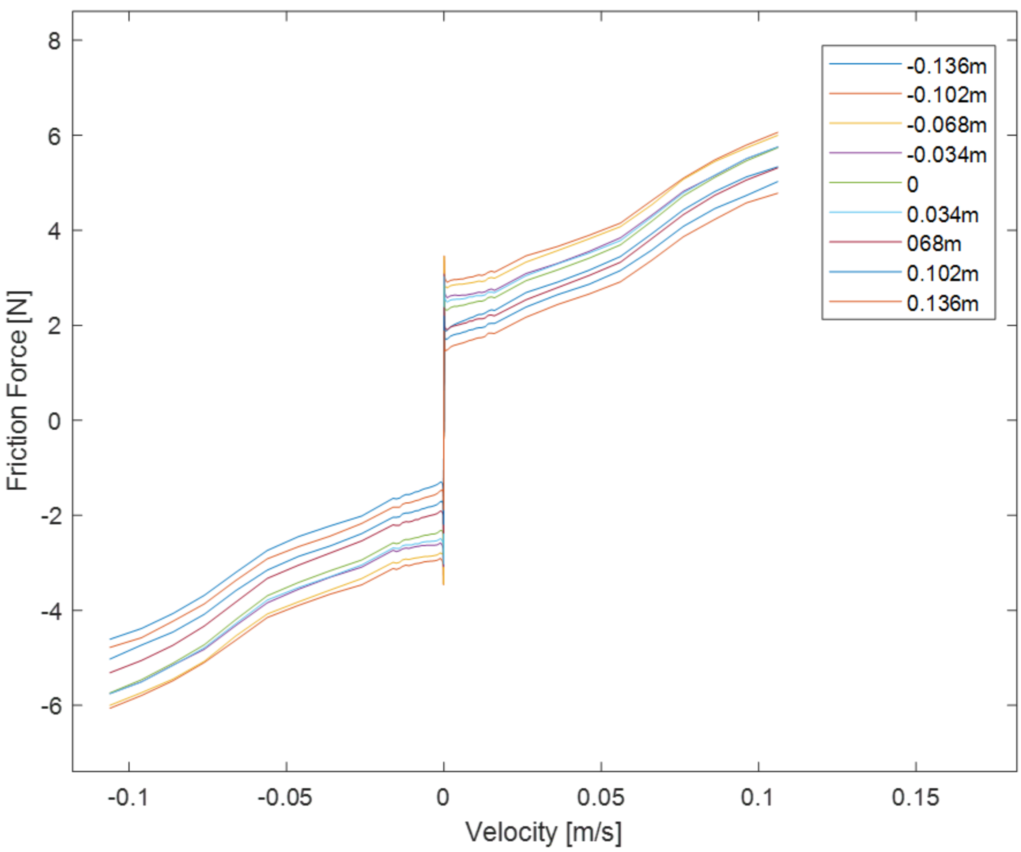

Figure 4.8: Velocity-friction map for static parameter identification at different positions.

In Figure 4.8, the Stribeck effect is obvious at all positions, with different Columb forces and Stribeck forces. The rate of increase and the Stribeck velocities appear similar to all positions.

4.3.2. Identification

Same as in the simulation, the identification is conducted separately with positive velocities and negative velocities, and the results are averaged to obtain the final identification result. As in the simulation work, Levenberg–Marquardt algorithm is used to calculate the optimum parameter values as well, and the initial value of λ is set as 0.01, same as the `lsqcurvefit` function of MatLab, and the initial guesses of parameters F_S, F_C, v_0, σ_2 are chosen in the same manner as in simulation.

Using the v-F maps at 9 positions, the identification results of static parameters F_S, F_C, v_0, σ_2 are shown below:

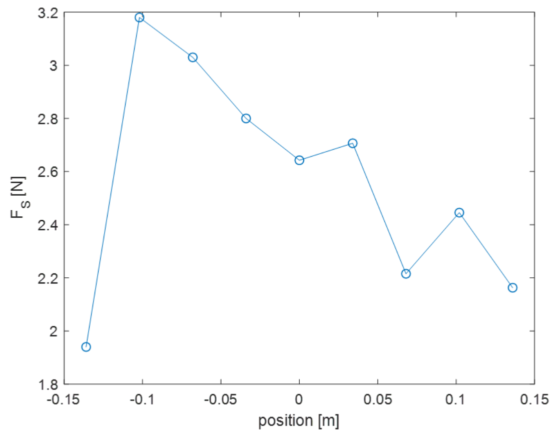

(a) Identification results of F_S at 9 positions.

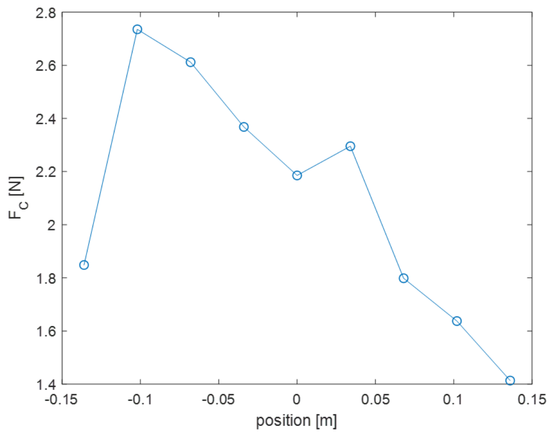

(b) Identification results of F_C at 9 positions.

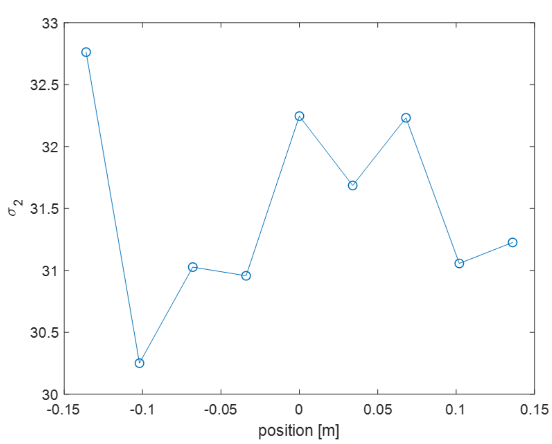

(c) Identification results of σ_2 at 9 positions.

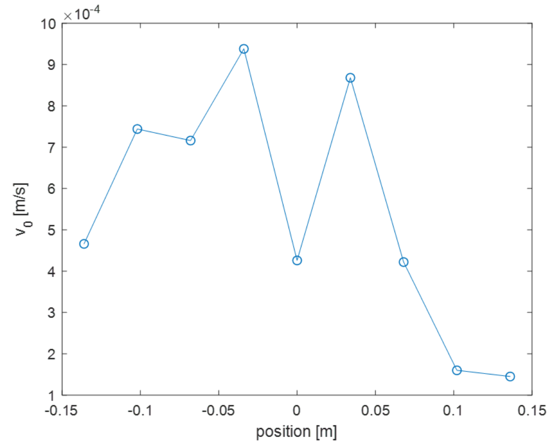

(d) Identification results of v_0 at 9 positions.

Figure 4.9: Identification results at 9 positions.

In Figure 4.9, for the static parameters F_S and $_C$, the parameters have a trend of decreasing from the position -0.102m. The trend of the parameters σ_2 and v_0 at different positions are not significant. The differences in the parameters at different positions are assumed to be caused by the inhomogeneously distributed lubrication on the track and the material of the track, thus different normal force along the track. The rate variance of identified values of v_0 is the largest among all parameters, one possible cause is that the measurement at near-zero velocity is affected by hysteresis dynamic friction phenomena.

To further analyze the result of identification, the residuals of the identified and the measured friction force are studied. Here the identification residuals at position 0 are shown as an example.

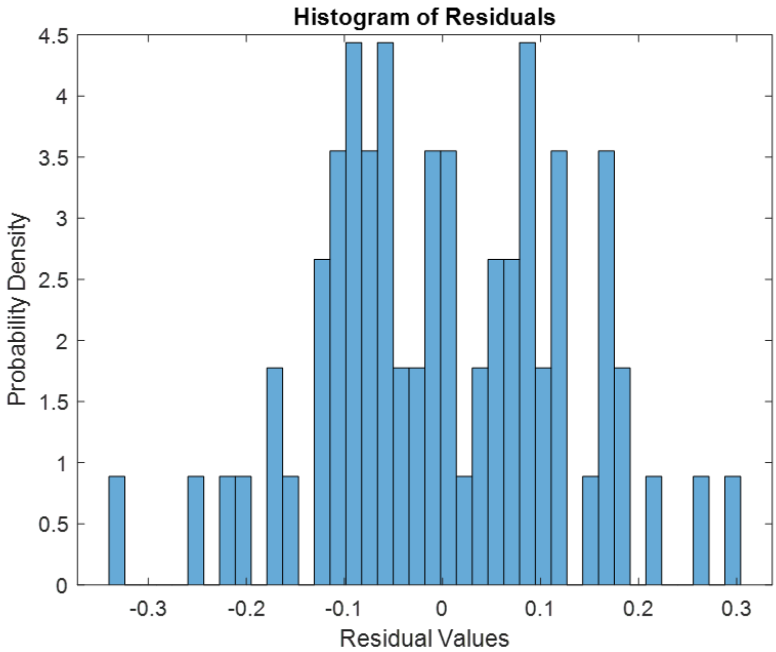

Figure 4.10: Histogram of residuals after identification at position 0.

From Figure 4.10 the histogram of residuals, the residuals after identification are slightly negatively biased, which means that lower estimations are more likely to happen. It can also be observed that the residuals do not follow a normal distribution or are also not centered to zero, and are more centered at -0.1 and 0.1.

The autocorrelation of residuals and cross-correlation between residuals and measured friction force are shown in Figure 4.11, where the red dotted lines represent the confidence of 90%. From Figure 4.11(a), most data points fall within the confidence intervals, and the residuals resemble random noise. The near-sinusoidal wave and the repeat spikes in both Figure 4.11 (a) and (b) indicate that the LuGre model does not account for all the underlying structures, which is explained in the model comparison chapter.

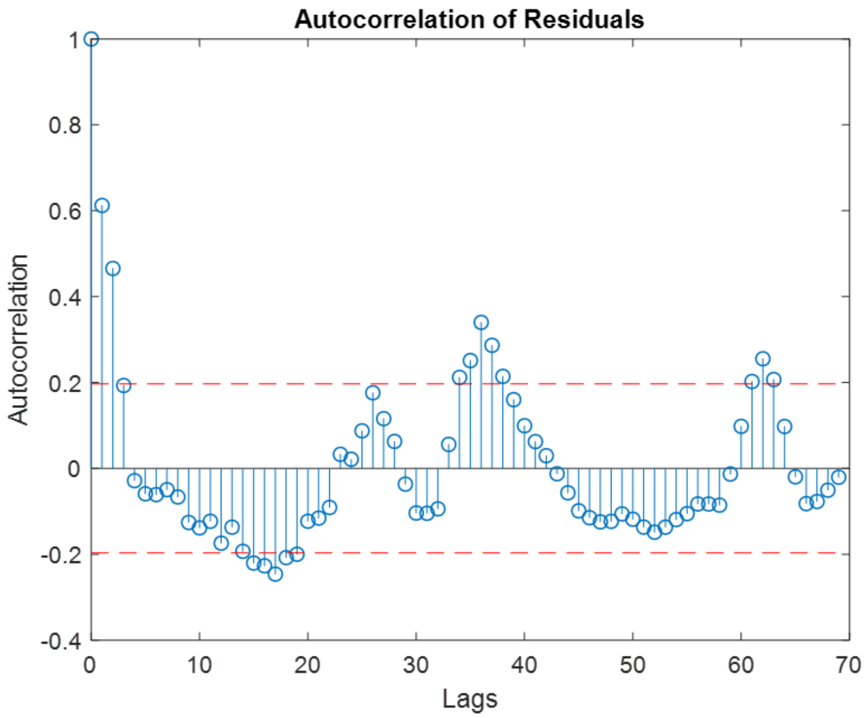

(a) Autocorrelation of residuals.

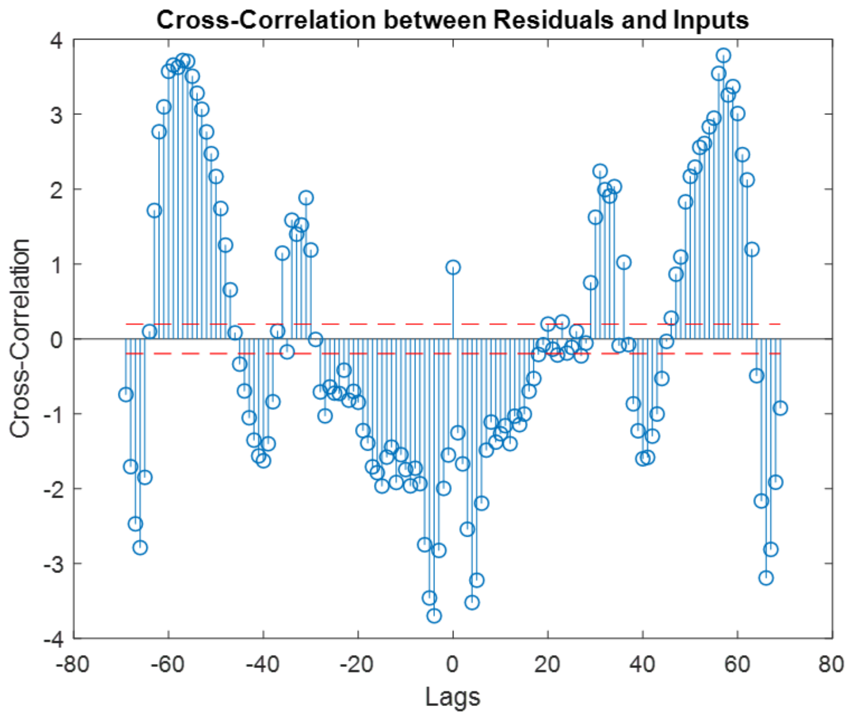

(b) Cross-correlation between residuals and measured friction forces.

Figure 4.11: Analysis of identification result at position 0.

4.4. Dynamic parameter experiments

4.4.1. Direct identification under the closed-loop control system

In the simulation work, the velocity reversal is realized by simulating a sinusoidal velocity with a very small gain. However, in the experimental setup, it is more realistic to control the carrier to move back and forth for a small distance by a closed-loop control system. The actuator force that can ensure the carrier moves in the most effective way is the control output of the control system. The carrier is controlled to move back and forth for a distance of 4um 50 times, the velocity at the end of each time is -0.001m/s and 0.001m/s for positive and negative movements, respectively.

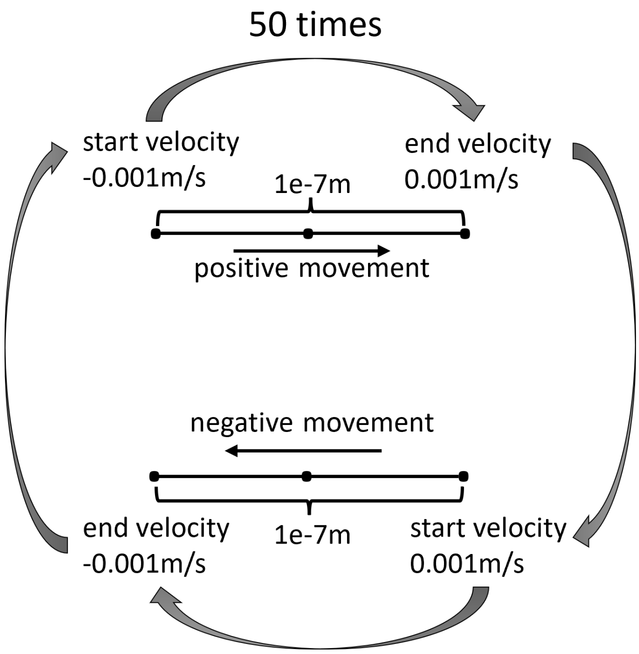

Figure 4.12: Closed-loop experiments to achieve velocity reversal.

During the 50 times velocity reversals, the velocity and the position in the time domain are shown as follows:

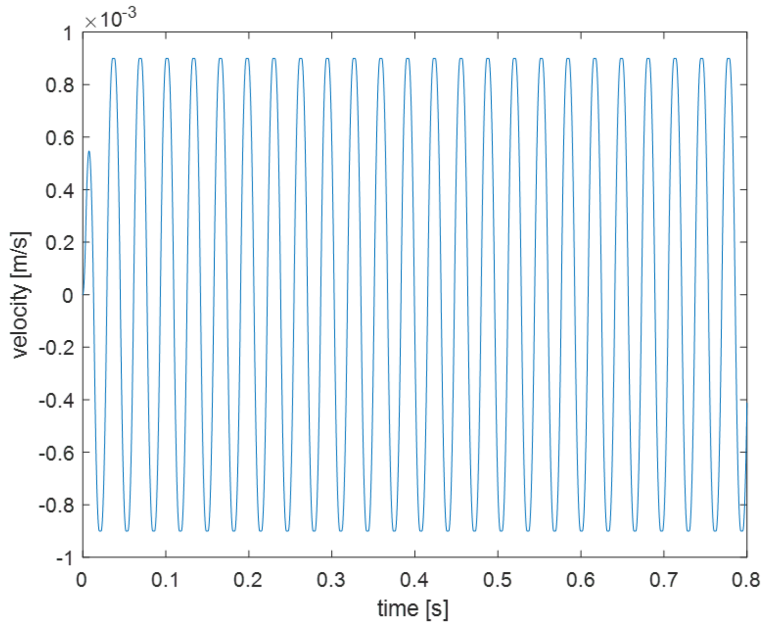

(a) Velocity in the time domain under closed-loop control system.

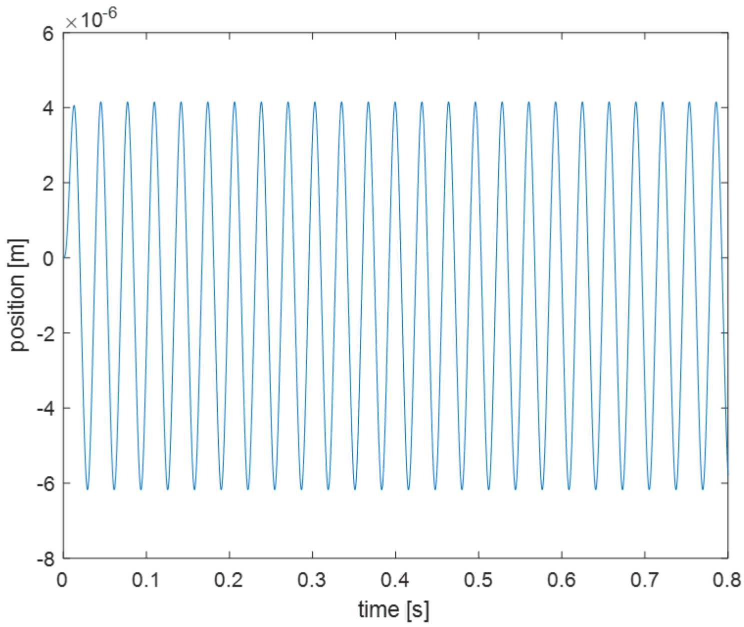

(b) Position in the time domain under closed-loop control system.

Figure 4.13: Closed-loop experiment for dynamic parameters.

The dynamic friction force is calculated using (4.1) by subtracting the actuator force and cable slab force from the inertia. In Figure 4.14, the measured friction force is represented by blue dots, and the red line shows the identified friction force using the LM algorithm based on the identification results of static parameters. It is obvious that compared to the hysteresis circle in Figure 3.4, the shape of the friction force curve in Figure 4.14 is unsuitable to be identified using the LuGre model. Because the closed-loop experiment on dynamic phenomena heavily depends on the design of the control system. To design effective control strategies, closed-loop control systems require a known or approximated model of the system's dynamics, which is unknown in this experiment. Closed-loop experiments are heavily reliant on accurate control system design, and create significant challenges when dealing with dynamic friction's nonlinear and time-varying characteristics, making open-loop experiments the preferred choice for parameter identification in this context.

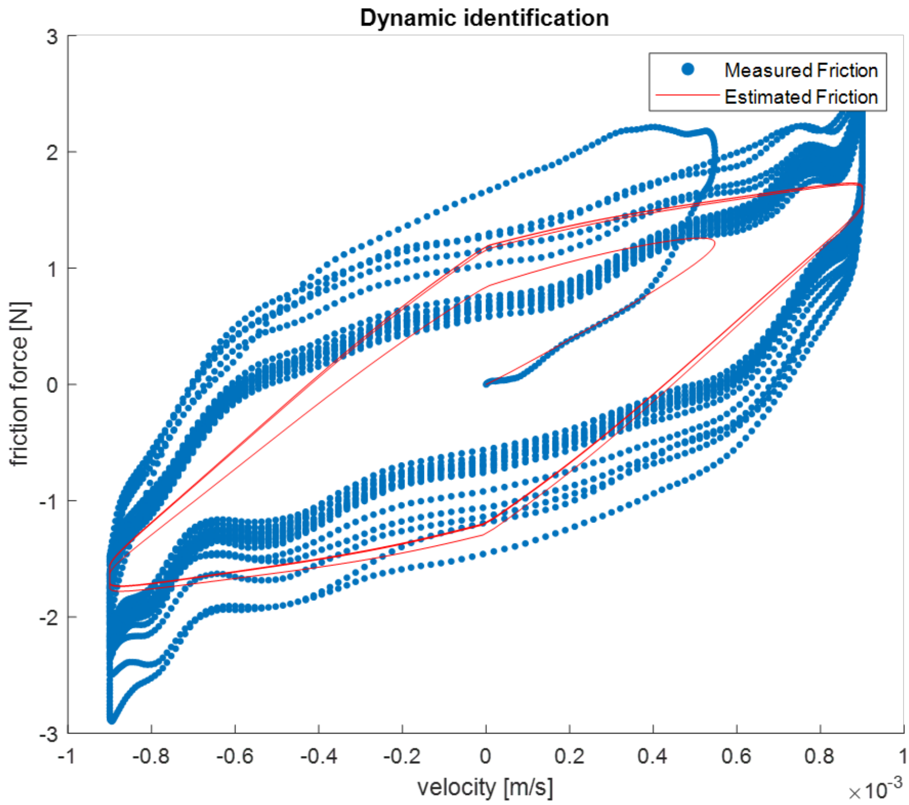

Figure 4.14: Identification of dynamic friction under closed-loop control system at position 0.

4.4.2. Inverse identification under the open-loop control system

To better capture the friction force at the velocity reversals, in real-world experiments, the inverse identification method under the open-loop control system is adopted[22][29]. In the open-loop control system, the actuator force is programmed to be sinusoidal with a gain of 2.136N, a frequency of 3s, and an offset of the cable force at the specific position. The sinusoidal actuator force empowers the carrier to move to positive and negative directions with small velocities, in this way, the velocity reversals are achieved. The data is sampled every 0.1 ms. The changes in velocity result in changes in positions, which can be demonstrated in the LuGre model and the system equation 4.1 by:

$$a * \frac{\mathrm{d}^2 p}{\mathrm{d}t^2} = F_{actuator} + f + F_{cable}; \tag{4.7}$$

$$\frac{\mathrm{d}z}{\mathrm{d}t} = v - \frac{\sigma_0 |v|}{F_C + (F_S - F_C) e^{-(\frac{v}{v_0})^{\frac{\sigma}{2}}}} z; \tag{4.8}$$

$$f = \sigma_0 z + \sigma_1 \frac{\mathrm{d}z}{\mathrm{d}t} + \sigma_2 v; \tag{4.9}$$

In this system model, p is the position of the carrier, the velocity $v = \mathrm{d}p/\mathrm{d}t$.

The parameter vector is $\sigma = [\sigma_0 \quad \sigma_1]$, The identification problem can be formulated as follows:

$$\min_{\mathbf{x}} c(\mathbf{x}), \tag{4.10}$$

$$\text{where} \quad c(\mathbf{x}) = \sum_{k=1}^{m} (p_{\text{measure}}(k) - p_{\text{output}}(\hat{\sigma}, k))^2, \tag{4.11}$$

where $\hat{\sigma}$ is the estimated parameter vector, and m is the number of sampled positions.

The Ordinary Differential Equation (ODE45) solver in MATLAB is used in the objective function. The presence of an ODE solver in the cost function introduced complexities in computing first and second derivatives because of its non-smoothness. These characteristics posed challenges for the Levenberg-Marquardt algorithm's gradient-based approach. On the contrary, the Simplex method's characteristic of direct search and its exploratory approach enabled it to navigate the discontinuous optimization problem with greater efficacy, resulting in improved convergence and better parameter estimation. Therefore, in the open-loop inverse identification of dynamic parameters, the Simplex search algorithm in the MATLAB optimization toolbox is chosen over the Levenberg-Marquardt algorithm.

4.4.3. Identification results

At nine positions ranging from -0.14m to 0.14m, which are the same as in the static parameter experiments, in the open loop system, a sinusoidal-shaped external force with a frequency of 3 s and a gain of 0.21 N is inserted into the carrier. The external force compensates the cable slab force with a bias that is manually tuned based on the identified cable slab force in the previous section. Under the influence of the inserted force, the carrier moves with small velocities in both directions, the velocity reversals are thus achieved. In the experiment window of 30s, the velocities and positions are measured. Using the Simplex search algorithm, the identified dynamic parameters σ_0 and σ_1 are obtained and shown in Figure 4.15, and estimated positions are shown in Figure 4.16 with the position 0.102m as an example.

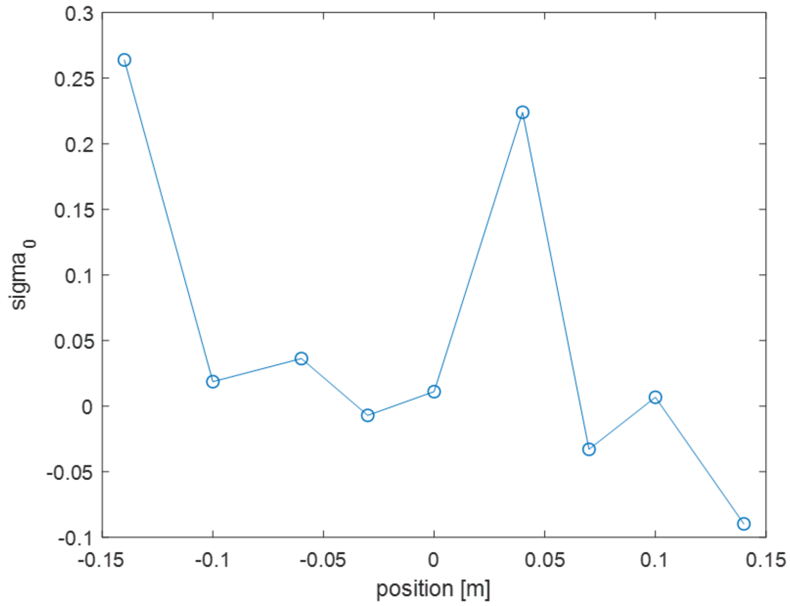

(a) Identification results of σ_0 at 9 positions.

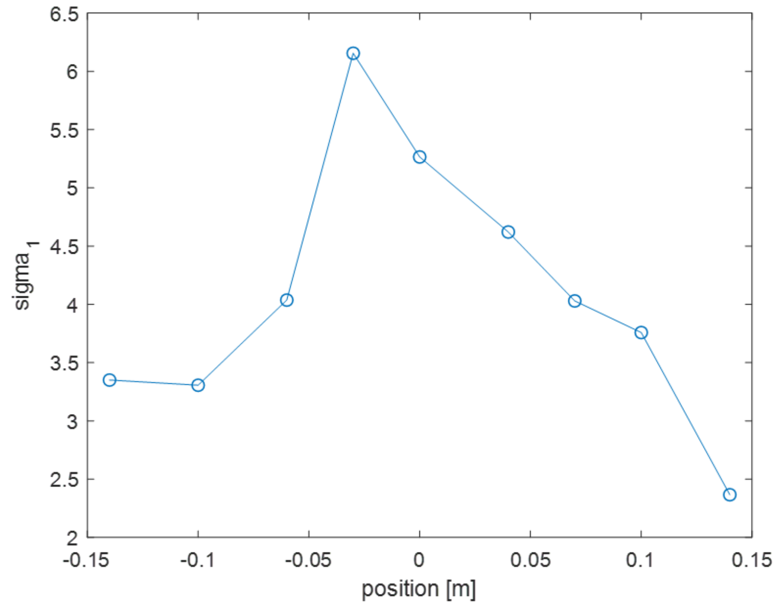

(b) Identification results of σ_1 at 9 positions.

Figure 4.15: Identification results at 9 positions.

Figure 4.16 shows that under the sinusoidal force, the velocity and position move with the same frequency as the force. The position has a transition time of one period, where the carrier moves closer to the starting point. With an accurate compensation of cable slab force, the position after the transition period has a fixed maximum/minimum point. The estimate fits better after the transition period than within the transition period.

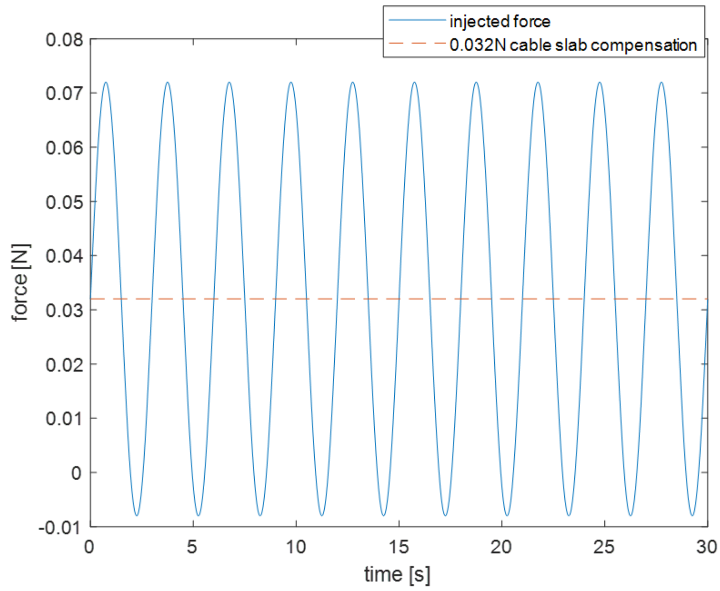

(a) Injected sine-shaped force.

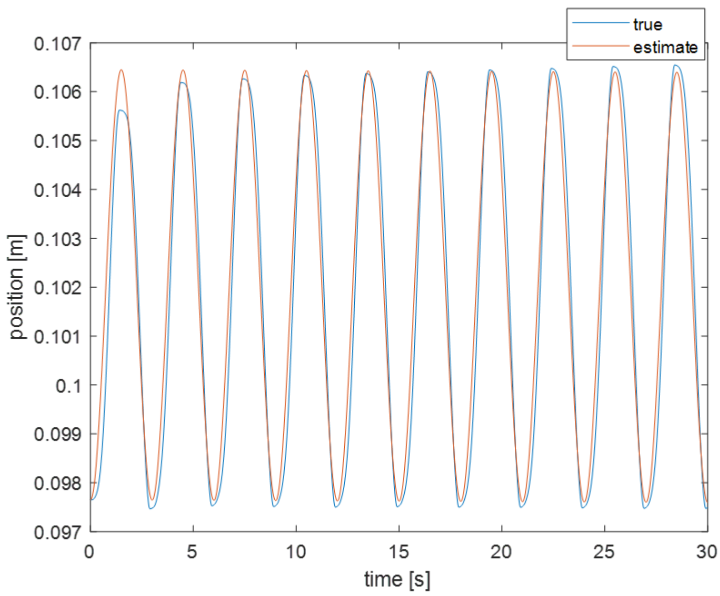

(b) Identified and measured position for dynamic parameters at position 0.102m.

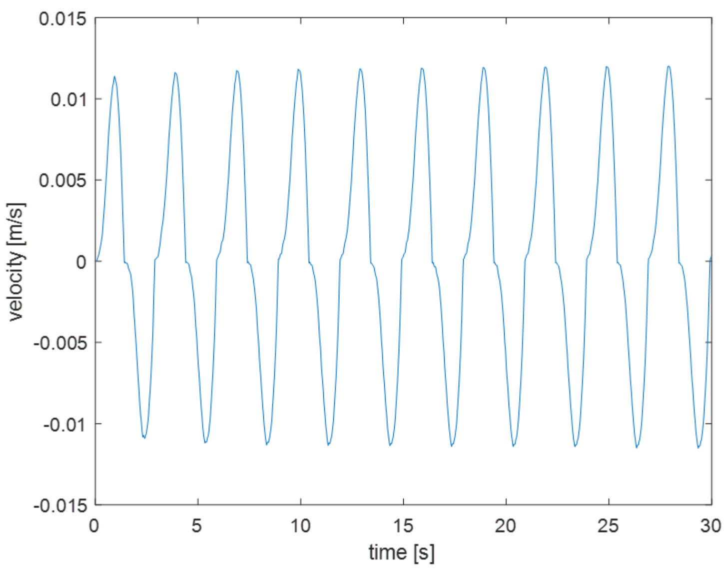

(c) Measured velocity for dynamic parameters at position 0.102m.

Figure 4.16: Identification results at 0.102m

To understand the identification results better, the residuals of the identified position and the measured position are analyzed. In the analyze work, the identification at position 0.102m is taken as an example.

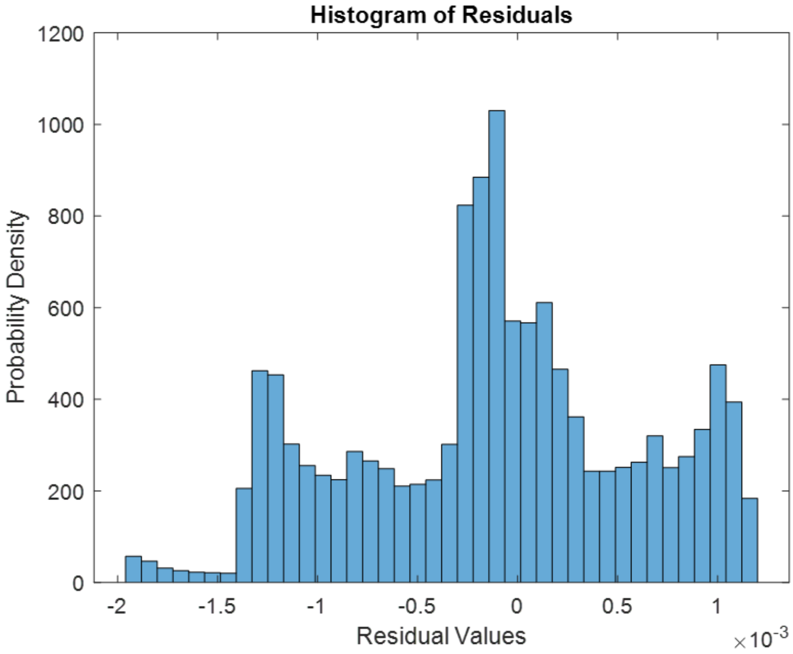

Figure 4.17: Histogram of residuals after identification at position 0.102.

From Figure 4.17 the histogram of residuals, the distribution of the residuals resembles normal distribution. It can also be seen that the distribution is slightly negatively biased, which can be explained in Figure 4.16(b) in the transition area, where the estimated position is significantly smaller than the measured position.

Figure 4.18 shows the autocorrelation of residuals and cross-correlation between residuals and measured positions. In both sub-figures, the red dotted lines represent the confidence of 90%. From Figure 4.18, the autocorrelation figure shows that the residuals are highly autocorrelated and highly cross-correlated, indicating that there is a persistent structure or pattern in the model's errors. This suggests that the model may not fully capture all the dynamics and there may be higher-order dynamics, nonlinearities, or unmodeled disturbances that are affecting the system.

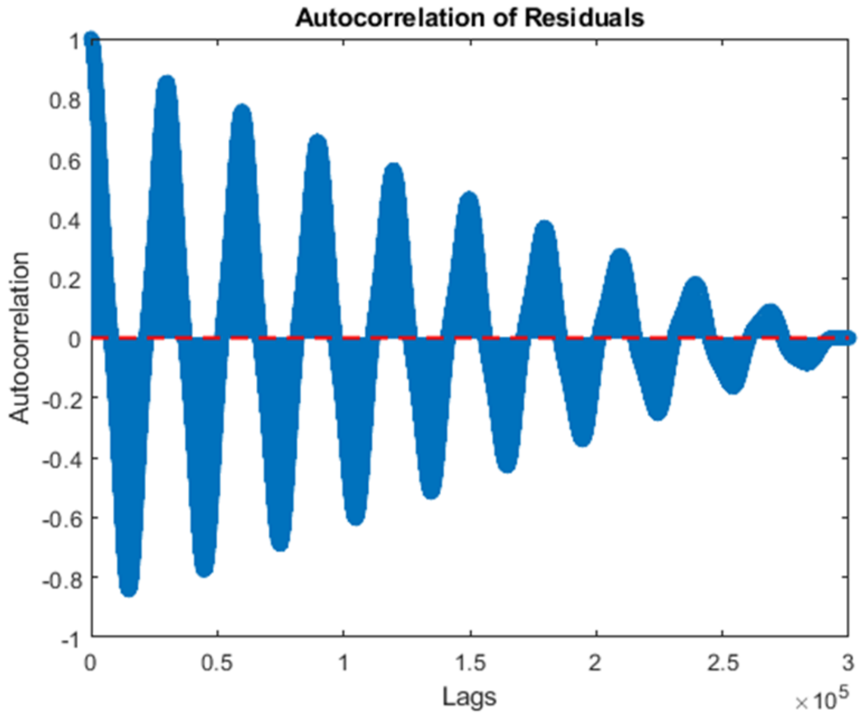

(a) Autocorrelation of residuals.

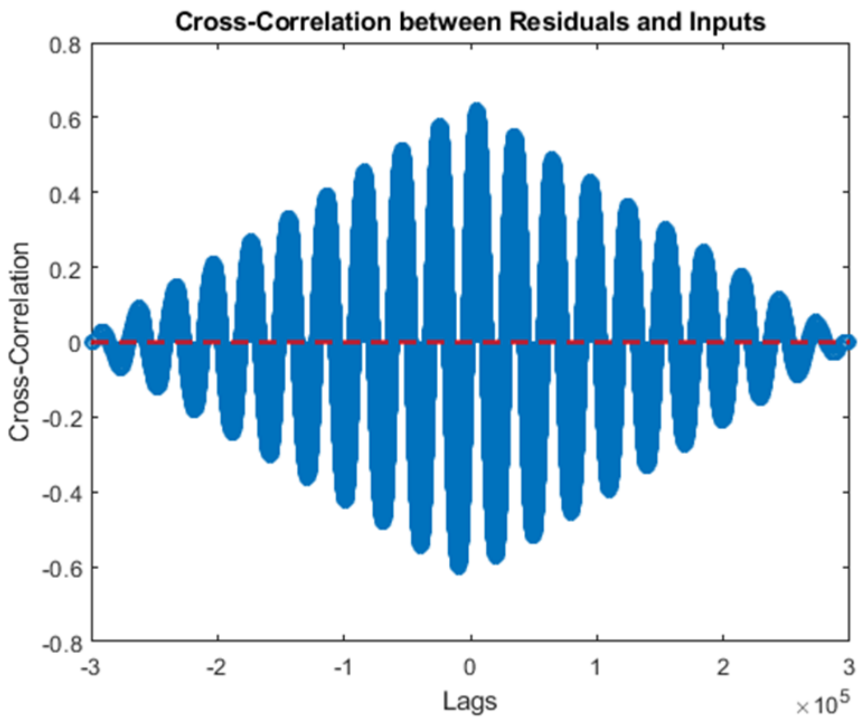

(b) Cross-correlation between residuals and measured positions.

Figure 4.18: Analysis of identification result at position 0.102..

4.5. Summary

This chapter provides a practical investigation into friction modeling on the Proton Motion Stage. First, a detailed introduction of the experimental setup is explained. Then, the chapter proceeds to the identification of cable slab forces and the demonstration of their position-dependent nature. Subsequently, static parameter identification experiments at different positions are conducted, revealing variations likely linked to material properties and lubrication along the motion track. The chapter then delves into dynamic parameter experiments, comparing closed-loop and open-loop control approaches, with the latter successfully identifying dynamic parameters σ_0 and σ_1.

5 Conclusions and Future Work

This research addresses the identification of friction force in the domain of precision engineering. Focusing on the Proton Motion Stage, this study selected the LuGre friction model and performed parameter identification in both simulation and experiments to gain a better understanding of the friction behavior and parameter identification on the Proton Motion Stage.

The thesis work accomplished the goals set in the introduction chapter as follows:

- **Literature Review and Model Selection: From the existing friction models used in precision engineering systems, select an appropriate model for further investigation.**

  The selection of model-based identification as the core approach for its capacity to provide a structured and comprehensive understanding of friction behavior. The model evaluation procedure involves static and dynamic friction models including the Stribeck model, LuGre, Leuven, modified Leuven, and Generalized Maxwell-Slip (GMS) models, based on the coverage of static and dynamic friction behavior, the required identification effort, and accuracy. Because the LuGre friction model incorporates both static and dynamic friction phenomena and requires achievable identification difficulty, LuGre is chosen as the model for further friction identification, despite the lack of non-local memory.

- **Simulations: Develop a computational model of the Proton Motion Stage that incorporates the selected friction model. Simulate the behavior of the system to explore the effects of different parameters and gain insights into friction dynamics.**

  Based on the LuGre friction model, simulation work is conducted using data generated using a trajectory generator tailored for the Proton Motion Stage. Through the incorporation of the LuGre friction model and identification of its parameters, the Stribeck effect and hysteresis dynamic phenomena are captured. The simulation work not only explored the frictional behaviors across a wide range of velocities but also provided sensitivity analysis on parameters, and disclosed the relative significance of each parameter in influencing friction force. The simulation work confirms the effectiveness of the LuGre friction model and the identification method and guides subsequent experimental procedures and identification using the real-world scenario.

- **Experimental Investigations: Perform a series of experiments on the Proton Motion Stage to identify friction parameters. This includes friction coefficient analysis and the study of position-dependent effects on friction forces.**

  The experimental investigations explored friction behavior within the Proton Motion Stage. The position-dependent cable slab force is investigated, and the effects of the force spikes caused by the bearing rolls entering and exiting the pressure zone are shown. For the identification of static friction force, the experiments utilized the same method as in the simulation work. The static parameters F_S,

F_C, v_0, and σ_2 at 9 positions away from the force spike areas are identified. For dynamic parameters σ_0 and σ_1, the experiment work compares the closed-loop and open-loop methods, which provides insights into the forward and inverse approach to the identification problem. Finally, under the open-loop control system, with the injection of sinusoidal force, the dynamic parameters at 9 positions are identified using the Simplex pattern search method. By analyzing the identification residuals of static and dynamic parameters, the thesis concludes that the LuGre model does not fully capture friction behavior, especially dynamic friction.

- **Comparison and Insights: Compare the findings from simulations and experimental investigations to have a deeper understanding of friction identification and friction behavior in the Proton Motion Stage.**

  In light of the findings and implications presented in this thesis, the following recommendations are suggested for future research and practical implementation:

  – **Enhance Friction Model Accuracy**: Given the limitations of the LuGre friction model in describing nonlinear friction forces, consider exploring modifications to improve model accuracy, including the evaluation of the GMS friction model's potential effectiveness, and extending the LuGre model to include additional parameters of terms that capture the hysteresis effects better.

  – **Multi-Model Investigation**: Explore the possibility of combining multiple friction models, such as the LuGre model and the modified Leuven model, to capture a broader range of friction behaviors and improve overall model accuracy, especially under varying operating conditions.

  – **Additional Data Collection**: Acquire additional data specifically designed to capture the behavior of the system at near-zero velocities. This may involve conducting experiments or measurements at extremely low speeds, where dynamic effects are more pronounced.

  – **Data-Driven Approaches**: Consider using data-driven approaches, such as machine learning algorithms, to predict and compensate for friction forces based on historical data and real-time sensor measurements, potentially enhancing the adaptability of the control scheme.

  – **Long-Term Stability and Reliability**: Perform long-term stability and reliability check of the proposed friction identification method, evaluating its performance over extended experimental periods and analyzing potential wear effects on friction behavior.

References

[1] T.H. Chiew et al. “Identification of Friction Models for Precise Positioning System in Machine Tools”. In: *Procedia Engineering* 53 (2013). Malaysian Technical Universities Conference on Engineering amp;amp; Technology 2012, MUCET 2012, pp. 569–578. DOI: https://doi.org/10.1016/j.proeng.2013.02.073. URL: https://www.sciencedirect.com/science/article/pii/S1877705813001926.

[2] H. Olsson et al. “Friction Models and Friction Compensation”. In: *European Journal of Control* 4.3 (1998), pp. 176–195. DOI: https://doi.org/10.1016/S0947-3580(98)70113-X. URL: https://www.sciencedirect.com/science/article/pii/S094735809870113X.

[3] B Armstrong-Helouvry et al. “Survey of models, analysis tools and compensation methods for the control of machines with friction”. In: *Automatica* 30.7 (July 1994). DOI: 10.1016/0005-1098(94)90209-7. URL: https://www.osti.gov/biblio/101944.

[4] R.W. Daniel. “Control of machines with friction: Brian Armstrong-Hélouvry”. In: *Automatica* 28.6 (1992), pp. 1285–1287. DOI: https://doi.org/10.1016/0005-1098(92)90076-R. URL: https://www.sciencedirect.com/science/article/pii/000510989290076R.

[5] C. Canudas de Wit et al. “A new model for control of systems with friction”. In: *IEEE Transactions on Automatic Control* 40.3 (1995), pp. 419–425. DOI: 10.1109/9.376053.

[6] J. Swevers et al. “An integrated friction model structure with improved presliding behavior for accurate friction compensation”. In: *IEEE Transactions on Automatic Control* 45.4 (2000), pp. 675–686. DOI: 10.1109/9.847103.

[7] V. Lampaert et al. “Modification of the Leuven integrated friction model structure”. In: *IEEE Transactions on Automatic Control* 47.4 (2002), pp. 683–687. DOI: 10.1109/9.995050.

[8] F. Al-Bender et al. “The generalized Maxwell-slip model: a novel model for friction Simulation and compensation”. In: *IEEE Transactions on Automatic Control* 50.11 (2005), pp. 1883–1887. DOI: 10.1109/TAC.2005.858676.

[9] Farid Al-Bender et al. “Characterization of friction force dynamics”. In: *IEEE Control Systems Magazine* 28.6 (2008), pp. 64–81. DOI: 10.1109/MCS.2008.929279.

[10] Tijani Ismaila B. et al. “Artificial Intelligent Based Friction Modelling and Compensation in Motion Control System”. In: *Advances in Mechatronics*. Ed. by Horacio Martinez-Alfaro. Rijeka: IntechOpen, 2011. Chap. 3. DOI: 10.5772/23432. URL: https://doi.org/10.5772/23432.

[11] Yannick Desplanques. “Amontons-Coulomb Friction Laws, A Review of the Original Manuscript”. In: *SAE International Journal of Materials and Manufacturing* 8.1 (2015), pp. 98–103. URL: http://www.jstor.org/stable/26268696 (visited on 08/30/2023).

[12] Morin A. J. “New Friction Experiments carried out at Metz in 1831-1833”. In: *Proceedings of the French Royal Academy of Sciences* 4 (1833), pp. 1–128.

[13] D. P. Hess et al. “Friction at a Lubricated Line Contact Operating at Oscillating Sliding Velocities”. In: *Journal of Tribology* 112.1 (Jan. 1990), pp. 147–152. DOI: 10.1115/1.2920220. eprint: https://asmedigitalcollection.asme.org/tribology/article-pdf/112/1/147/5818931/147_1.pdf. URL: https://doi.org/10.1115/1.2920220.

[14] Osborne Reynolds. “On the Theory of Lubrication and Its Application to Mr. Beauchamp Tower’s Experiments, Including an Experimental Determination of the Viscosity of Olive Oil”. In: *Philosophical Transactions of the Royal Society of London* 177 (1886), pp. 157–234. URL: http://www.jstor.org/stable/109480 (visited on 08/23/2023).

[15] Ernest Rabinowicz. "The Nature of the Static and Kinetic Coefficients of Friction". In: *Journal of Applied Physics* 22.11 (Apr. 2004), pp. 1373–1379. DOI: 10.1063/1.1699869. eprint: https://pubs.aip.org/aip/jap/article-pdf/22/11/1373/7918013/1373_1_online.pdf. URL: https://doi.org/10.1063/1.1699869.

[16] A.Tustin. "The effects of backlash and of speed-dependent friction on the stability of closed-cycle control systems". In: *Journal of the Institution of Electrical Engineers* 94.1 (1947), pp. 143–151. DOI: https://doi.org/10.1049/ji-2a.1947.0021.

[17] Dahl P. R. "Solid friction model". In: *Technical Report TOR-0158 (3107-18)-1, Aerospace Corp El Segundo CA, Los Angeles Air Force Station* (1968).

[18] M. Gafvert. "Comparisons of two dynamic friction models". In: *Proceedings of the 1997 IEEE International Conference on Control Applications*. 1997, pp. 386–391. DOI: 10.1109/CCA.1997.627584.

[19] Robert Rens Waiboer. "Dynamic modelling, identification and simulation of industrial robots: for off-line programming of robotised laser welding". English. PhD thesis. Netherlands: University of Twente, Feb. 2007. DOI: 10.3990/1.9789077172254.

[20] Demosthenis D. Rizos et al. "FRICTION IDENTIFICATION BASED UPON THE LUGRE AND MAXWELL SLIP MODELS". In: *IFAC Proceedings Volumes* 38.1 (2005). 16th IFAC World Congress, pp. 548–553. DOI: https://doi.org/10.3182/20050703-6-CZ-1902.00092. URL: https://www.sciencedirect.com/science/article/pii/S1474667016361043.

[21] A. Amthor et al. "FRICTION IDENTIFICATION AND COMPENSATION ON NANOMETER SCALE". In: *IFAC Proceedings Volumes* 41.2 (2008). 17th IFAC World Congress, pp. 2014–2019. DOI: https://doi.org/10.3182/20080706-5-KR-1001.00342. URL: https://www.sciencedirect.com/science/article/pii/S1474667016392473.

[22] C. Canudas de Wit et al. "Adaptive friction compensation with partially known dynamic friction model". In: *International Journal of Adaptive Control and Signal Processing* 11.1 (1997), pp. 65–80. DOI: https://doi.org/10.1002/(SICI)1099-1115(199702)11:1<65::AID-ACS395>3.0.CO;2-3. eprint: https://onlinelibrary.wiley.com/doi/pdf/10.1002/%28SICI%291099-1115%28199702%2911%3A1%3C65%3A%3AAID-ACS395%3E3.0.CO%3B2-3. URL: https://onlinelibrary.wiley.com/doi/abs/10.1002/%28SICI%291099-1115%28199702%2911%3A1%3C65%3A%3AAID-ACS395%3E3.0.CO%3B2-3.

[23] De-Peng Liu. "Research on parameter identification of friction model for servo systems based on genetic algorithms". In: *2005 International Conference on Machine Learning and Cybernetics*. Vol. 2. 2005, 1116–1120 Vol. 2. DOI: 10.1109/ICMLC.2005.1527110.

[24] E Rabinowicz. "The Intrinsic Variables affecting the Stick-Slip Process". In: *Proceedings of the Physical Society* 71.4 (Apr. 1958), p. 668. DOI: 10.1088/0370-1328/71/4/316. URL: https://dx.doi.org/10.1088/0370-1328/71/4/316.

[25] Friedhelm Altpeter et al. "Identification for Control of Drives with Friction". In: *IFAC Proceedings Volumes* 30.6 (1997). IFAC Conference on Control of Industrial Systems "Control for the Future of the Youth", Belfort, France, 20-22 May, pp. 529–533. DOI: https://doi.org/10.1016/S1474-6670(17)43418-5. URL: https://www.sciencedirect.com/science/article/pii/S1474667017434185.

[26] Kenneth Levenberg. "A method for the solution of certain non-linear problems in least squares". In: *Quarterly of Applied Mathematics* 2.2 (1944), pp. 164–168. DOI: 10.1090/qam/10666. URL: https://doi.org/10.1090%2Fqam%2F10666.

[27] Mark K. Transtrum et al. *Improvements to the Levenberg-Marquardt algorithm for nonlinear least-squares minimization*. 2012. arXiv: 1201.5885 [physics.data-an].

[28] S.J.L. Hoen. "Output feedback control of nonlinear motion systems with use of high-gain observers". MA thesis. Eindhoven: Eindhoven University of Technology, 2014.

[29] Meseret Abayebas Tadese et al. “Passivity Guaranteed Dynamic Friction Model With Temperature and Load Correction: Modeling and Compensation for Collaborative Industrial Robot”. In: *IEEE Access* 9 (2021), pp. 71210–71221. DOI: 10.1109/ACCESS.2021.3076308.